

Magnetic field amplification in collapsing, non-rotating stellar cores

M. Obergaulinger and H.-Th. Janka

¹ Max-Planck-Institut für Astrophysik, Karl-Schwarzschild-Str. 1, D-85748 Garching, Germany

² Racah Institute of Physics, The Hebrew University, Jerusalem 91904, Israel

Received xx month xxxx / Accepted xx month xxxx

ABSTRACT

Context. The influence of magnetic fields on stellar core collapse and explosion is not well explored. It depends on the possibility to amplify the initial pre-collapse fields. In the absence of rotation this can happen by compression, convection, the standing accretion shock instability, and the accumulation and growth of Alfvén waves in the accretion flows.

Aims. We investigate such amplification mechanisms of the magnetic field during the collapse and post-bounce evolution of the core of a non-rotating $15 M_{\odot}$ star with varied initial field strengths, taking into account the microphysical equation of state and neutrino physics that play a crucial role in supernova cores.

Methods. We perform simulations of ideal magnetohydrodynamics with neutrino transport in axisymmetry. The transport of electron neutrinos and antineutrinos is treated with a new scheme that solves the energy-dependent set of radiation energy and momentum equations in two dimensions by using an analytic closure relation.

Results. The magnetic field undergoes kinematic amplification by turbulent flows. We also find indications for amplification by interacting waves travelling upwards and downwards inside accretion streams. The fields can reach up to equipartition with the velocity field. Very high magnetic field strengths require very strong pre-collapse fields and are able to shape the post-bounce flow, leading to a pattern dominated by low-order multipoles. Such models are closest to a successful explosion.

Conclusions. Magnetic fields can build up to interesting strengths even in non-rotating collapsing stellar cores. Starting with fields in the pre-collapse core as predicted by present stellar evolution models (10^9 – 10^{10} G), typical neutron star fields of 10^{12} – 10^{13} G emerge, whereas progenitor fields of some 10^{11} – 10^{12} G lead to fields of magnetar strength of about 10^{14} – 10^{15} G. Only in the latter case the magnetic fields have significant dynamical effects on the flows in the supernova core and may have an influence on the explosion mechanism. However, in none of our 2D simulations, we find an explosion until 500 milliseconds post-bounce.

Key words. Magnetohydrodynamics (MHD) - Supernovae: general - Stars: magnetic fields - Stars: magnetars

1. Introduction

Most scenarios for the explosion mechanism of core-collapse supernovae (SNe) involve a combination of energy deposition in the matter surrounding the nascent proto-neutron star (PNS) and multi-dimensional hydrodynamic flows. Examples for means of energy transfer to the SN ejecta are the prompt bounce shock, neutrinos, magnetic fields and acoustic waves. In the neutrino-heating mechanism neutrinos tap the gravitational potential energy released during collapse and deposit a part of it behind the stalled shock. This process is enhanced and thus supported by non-radial fluid flows triggered by hydrodynamic instabilities like convection and the standing accretion shock instability (SASI; Blondin et al. 2003; Foglizzo 2001, 2002)

Though it is safe to assume that the exploding star will possess a magnetic field of some (unknown) strength and topology, its possible influence on the explosion is less clear. The main reason for the small number of conclusive investigations into this topic is that important effects are expected to occur only when the magnetic field is roughly in (energetic) equipartition with the gas flow, a condition corresponding to extremely strong fields similar to those observed in magnetars. This makes full MHD simulations including a treatment of the important neutrino physics in the SN core indispensable.

Stellar evolution calculations, predicting only weak pre-collapse magnetic fields, render the prospects for magneti-

cally affected explosions very much dependent on the amount of field amplification happening during and after collapse. Rapid rotation may amplify a weak seed field quite generically to dynamically relevant values, e.g., by winding up a poloidal field (a process linear in time) or, exponentially in time, by the magneto-rotational instability (MRI, Akiyama et al. 2003). Magneto-rotational explosions, theoretically discussed by Meier et al. (1976), have been studied in various approximations, e.g., by Bisnovatyi-Kogan et al. (1976); Symbalisty (1984); Akiyama et al. (2003); Kotake et al. (2004); Obergaulinger et al. (2006); Cerdá-Durán et al. (2007); Obergaulinger et al. (2009); recent simulations employing detailed microphysics have been performed by Burrows et al. (2007); Scheidegger et al. (2008).

However, according to stellar-evolution models, the majority of progenitors is expected to rotate slowly. Although many stars on the upper main sequence show a surface rotation period close to the critical value for mass shedding, they will most likely lose most of their angular momentum during their subsequent evolution, e.g., by strong stellar winds or magnetic braking (Heger et al. 2005; Meynet et al. 2011). Non-rotating cores, albeit lacking the above-mentioned efficient channels for amplification, may experience field growth by several effects:

1. After bounce, convection develops in the PNS and the surrounding hot-bubble region. Breaking down into three-dimensional turbulence, convection may provide the α effect

responsible for a small-scale dynamo amplifying the field on length scales comparable to the scale of turbulent forcing, i.e., the size of convective eddies (Thompson & Duncan 1993). However, the generation of a large-scale field, e.g., on the scale of the PNS, probably requires a non-vanishing kinetic helicity of the turbulent flow, which can most naturally be accounted for by (differential) rotation (see, e.g., Brandenburg & Subramanian 2005).

2. Endeve et al. (2010) have demonstrated that the standing-accretion-shock instability (SASI Blondin et al. 2003), excited by a feedback cycle of acoustic and advective perturbations travelling between the shock wave and the deceleration region above the PNS, has the potential to amplify the magnetic field by up to four orders of magnitude. Dynamically relevant field strengths (in which case the field reaches at least 10% of the equipartition strength) can be reached only when the pre-collapse field in the stellar core is sufficiently strong.
3. Non-radial fluid motions triggered by these instabilities can excite perturbations of the magnetic field propagating as Alfvén waves along the field lines. The outward propagation of Alfvén waves excited close to the PNS has to compete with the accretion of gas towards the centre. Assuming that the accretion flow decelerates in this region continuously, Guilet et al. (2010) argue that there must be an *Alfvén point* at which the Alfvén speed equals the accretion velocity, and the propagation of the wave (measured in the lab frame) comes to a rest. They show that Alfvén waves are amplified exponentially at such a stagnation point. At the conditions of a supernova core, the amplification should be most efficient for a magnetic field strength of a few 10^{13} G and could yield final fields of the order of 10^{15} G. Dissipation of the wave energy can increase the entropy of the gas, thus modifying the dynamics in the accretion region. For even stronger fields, the Alfvén point can be close to the shock wave. In this case, Suzuki et al. (2008) find that the explosion can be driven solely by the energy deposited by the dissipation of Alfvén waves. This process transmitting energy from the (convectively active) PNS to the much less dense surrounding medium bears a strong similarity to the proposed mechanism for heating the solar corona by Alfvén waves emerging from the solar surface.

Previous simulations of magnetohydrodynamic stellar core collapse have used a wide variety of methods to treat the effects of neutrinos: in the simplest models, they were either ignored (e.g., Obergaulinger et al. 2006; Mikami et al. 2008) or treated by simple parameterizations or local source terms (e.g., Cerdá-Durán et al. 2008); more complex approaches include trapping/leakage schemes (e.g., Kotake et al. 2004), multi-dimensional, energy-dependent flux-limited diffusion (Dessart et al. 2006) or the isotropic-diffusion source approximation which discriminates between trapped and free-streaming components (Liebendörfer et al. 2009). In our approach to radiation-magnetohydrodynamics (RMHD), we employ a new multi-dimensional and energy-dependent scheme for the neutrino transport in supernova cores, namely a two-moment solver for the neutrino energy (lepton number) and momentum equations with an analytic closure relation (Cernohorsky & van Weert 1992; Pons et al. 2000; Audit et al. 2002). Presently it includes only electron neutrinos and antineutrinos and a relatively simple treatment only of the most relevant interaction rates of these neutrinos with neutrons, protons, and nuclei. Nevertheless, in the context of the questions focussed on

Table 1. Variables and symbols used in the MHD equations and the neutrino transport formulation presented in this article.

Symbol	Variable
ρ	gas density
Y_e	electron fraction
\mathbf{v}	gas velocity
\mathbf{b}	magnetic field
ε	internal energy density
e_\star	total energy density
P	gas pressure
P_\star	total pressure
Φ	gravitational potential
S_ν^0	neutrino-matter energy exchange
$S_{\nu;n}^0$	neutrino-matter lepton-number exchange
S_ν^i	neutrino-matter momentum exchange
E_ν	neutrino energy density
N_ν	neutrino number density
F_ν^i	neutrino energy flux
V_ν^i	neutrino number flux
p_ν	scalar Eddington factor
P_ν^{ij}	neutrino energy pressure tensor
R_ν^{ij}	neutrino number pressure tensor
χ^0	0 th -moment opacity
χ^1	1 st -moment opacity

in this paper, the scheme provides a reasonably good representation of the neutrino effects that play a role during core collapse, bounce, shock propagation and in the accretion layer behind the stalled supernova shock. Moreover, it is a computationally efficient treatment of the neutrino transport, and two-dimensional simulations up to several hundred milliseconds after bounce are easily possible.

It is the goal of this work to investigate the relevance of field amplification mechanisms like those in points 1.-3. concerning their importance for the evolution and potential revival of the stalled shock by core-collapse simulations including a reasonably good treatment of the relevant microphysics. In particular, we will study the field growth connected to convective and SASI activity in the post-shock layer and the role of energy transport and dissipation by Alfvén waves. To this end, we perform MHD simulations of collapse and post-bounce evolution of the core of a star of 15 solar masses (Woosley et al. 2002). Varying the strength of the initial field, assumed to be purely poloidal, we can determine different sites and mechanisms of field amplification and identify the back-reaction of the field onto the flow.

This article is organised as follows: Sect. 2 describes our physical model and the numerical methods; Sect. 3 introduces the initial conditions; Sect. 4 presents the results of our simulations; Sect. 5 gives a summary of the study and draws some conclusions; appendix A gives a brief overview of our treatment of the neutrino transport.

2. Physical model and numerical methods

2.1. Magnetohydrodynamics

We assume that the evolution of the gas and the magnetic field is described by the equations of Newtonian ideal magnetohydrodynamics (MHD),

$$\partial_t \rho + \nabla \cdot (\rho \mathbf{v}) = 0, \quad (1)$$

$$\partial_t (\rho Y_e) + \nabla \cdot (\rho Y_e \mathbf{v}) = S_{\nu;n}^0, \quad (2)$$

$$\partial_t (\rho v^j) + \nabla_j (P_\star \delta^{ij} + \rho v^i v^j - b^i b^j) = \rho \nabla^i \Phi + S_\nu^i, \quad (3)$$

$$\partial_t e_\star + \nabla \cdot ((e_\star + P_\star)\mathbf{v} - (\mathbf{v} \cdot \mathbf{b})\mathbf{b}) = \rho \mathbf{v} \cdot \nabla \Phi + S_\nu^0, \quad (4)$$

$$\partial_t \mathbf{b} - \nabla \times (\mathbf{v} \times \mathbf{b}) = 0, \quad (5)$$

describing the conservation of mass, electron fraction, gas momentum, total energy of the matter, and magnetic flux, respectively. In addition to these evolutionary equations, the magnetic field has to fulfil the divergence constraint,

$$\nabla \cdot \mathbf{b} = 0. \quad (6)$$

The symbols used in this system have standard meaning; they are listed in Tab. 1. The total energy density and pressure are defined as the sum of the contributions of the gas and the magnetic field, $e_\star = \varepsilon + 1/2 \rho v^2 + 1/2 \mathbf{b}^2$ and $P_\star = P + 1/2 \mathbf{b}^2$, respectively.

The MHD part of the system is closed by the equation of state of Shen et al. (1998), relating gas density, internal-energy density, and electron fraction to temperature, T , gas pressure P , entropy, S , the composition of four species (neutrons, protons, α particles, and a representative heavy nucleus), and the chemical potentials of neutrons, protons, and electrons.

To include some key features of general relativity into our Newtonian model, we use the modified gravitational potential of Marek et al. (2006). Following the lines proposed by these authors, we include the gas and neutrino energy density and pressure as well as an approximate Lorentz factor of the flow in the source term of the Poisson equation for Φ . Overall, this leads to a somewhat deeper potential well when the core approaches nuclear matter density and serves as a good approximation to the stronger relativistic gravity of a PNS.

Our code is based on an implementation of the MHD equations on a fixed Eulerian grid in the constrained-transport discretisation (Evans & Hawley 1988). It uses *high-resolution shock-capturing (HRSC)* methods with approximate Riemann solvers (Lax-Friedrichs, HLL, or HLLD (Miyoshi & Kusano 2005)) in the multi-stage framework (Titarev & Toro 2005). We reconstruct the conserved variables using high-order *monotonicity-preserving (MP)* methods (Suresh & Huynh 1997). Time stepping is done by explicit Runge-Kutta schemes of 2nd, 3rd, or 4th order.

2.2. Neutrino transport and neutrino-matter interactions

We treat the transport of neutrinos by solving the energy-dependent, multi-dimensional moment equations for neutrino energy, E_ν , and neutrino momentum, F_ν^i ,

$$\partial_t E_\nu + \nabla \cdot (E_\nu \mathbf{v} + \mathbf{F}_\nu) - \omega \nabla_j v_k \partial_\omega P_\nu^{jk} = S_\nu^0, \quad (7)$$

$$\partial_t F_\nu^i + \nabla_j (F_\nu^i v^j + P_\nu^{ij}) + F_\nu^i \nabla_j v^j = S_\nu^{1:i}. \quad (8)$$

Presently only electron neutrinos, ν_e , and antineutrinos, $\bar{\nu}_e$ are considered. The source terms, $S_\nu^{0,1}$, include the interaction of neutrinos with the gas by emission, absorption, and scattering reactions; we use a reduced set of processes, viz.

1. emission and absorption of electron neutrinos by neutrons,
2. emission and absorption of electron anti-neutrinos by protons,
3. elastic scattering of all neutrinos off nucleons,
4. emission and absorption of electron neutrinos by heavy nuclei,
5. coherent elastic scattering of all neutrinos off heavy nuclei.

Furthermore, fluid-velocity dependent effects such as the $P dV$ work associated with diverging flows appear in the equations as well. To close the system of moment equations, we have to

Table 2. Average magnetic field strengths and normalised magnetic energies for our computed models with magnetic field (excluding model s15-B0). See text for details.

model	s15-B10	s15-B11	s15-B11.5	s15-B12
b_0	10^{10}	10^{11}	3.16×10^{11}	10^{12}
b_{14} [G]	1.2×10^{13}	1.4×10^{14}	4.2×10^{14}	1.4×10^{15}
β_{14}^i	5.9×10^{-9}	7.8×10^{-7}	7.5×10^{-6}	5.9×10^{-5}
β_{14}^k	0.20	24	82	700
b_{cnv} [G]	9.1×10^{12}	1.2×10^{14}	2.1×10^{14}	4.7×10^{14}
β_{cnv}^i	1.1×10^{-7}	2.9×10^{-5}	9.8×10^{-5}	4.8×10^{-4}
β_{cnv}^k	0.00041	0.055	0.16	1.6
b_{stb} [G]	3.8×10^{12}	3.0×10^{13}	6.3×10^{13}	1.4×10^{14}
β_{stb}^i	1.1×10^{-6}	7.8×10^{-5}	3.3×10^{-4}	1.4×10^{-3}
β_{stb}^k	0.0020	0.16	0.80	3.7
b_{gain} [G]	3.6×10^{11}	6.0×10^{12}	1.0×10^{13}	1.2×10^{13}
β_{gain}^i	2.2×10^{-6}	5.7×10^{-4}	2.7×10^{-3}	1.0×10^{-2}
β_{gain}^k	0.000089	0.016	0.071	0.26

specify the tensor of the second moment, P_ν^{ij} , for which we use a simple analytic closure relation from Minerbo (1978). Using a tensorial generalisation of a one-dimensional *Eddington factor*, our method is generically multi-dimensional. A more detailed discussion can be found in Appendix A.

We note that our set of equations is a generalisation of the usual diffusion ansatz, in which the system of moment equations is truncated at the level of the energy equation and closed by expressing the flux in terms of the gradient of the energy density, mostly connecting diffusion and free-streaming limits by a flux limiter. Retaining the first two moments, it leads to a hyperbolic system, which can be solved by common methods such as high-resolution shock-capturing methods. More details on this can be found in Appendix A.

3. Models and initial conditions

Interested in the contribution of magnetic fields to the dynamics of supernovae, we simulate the evolution of a star of 15.0 solar masses with solar metallicity (Woosley et al. 2002). We map the pre-collapse model to a grid of $n_r = 320$ radial zones distributed logarithmically over a radial domain of [$r_{\min} = 0$; $r_{\max} \approx 2800$ km] and $n_\theta = 64$ lateral zones distributed uniformly between the north and south pole. The resolution at the grid centre is $(\delta r)_{\text{ctr}} = 400$ m. Ten energy bins between $\epsilon_{\min} = 0.1$ MeV and $\epsilon_{\max} = 280$ MeV are used for the neutrinos.

The topology of the magnetic field at the onset of collapse is highly uncertain. On the main sequence, field amplification by, e.g., gradual contraction of the star or convection competes with the loss of magnetic energy in stellar winds and in work the magnetic field does by exerting torques on the stellar matter. In the absence of rotation, stars lack an important ingredient of most large-scale dynamos. In such a case, they may be dominated by a small-scale turbulent field rather than a large-scale field, e.g., a lower-order multipole. Nevertheless, we assume a simple initial field, viz. a modified dipole (Fig. 1). While this is probably not a very good approximation to real stellar cores, it represents an optimal configuration for the Alfvén-wave amplification mechanism we are interested in because of the large coherent radial component favouring the radial propagation of Alfvén waves. Furthermore, we observe that the field is replaced by a more complex small-scale field in the regions of the core affected by hydrodynamic instabilities such as convection and the

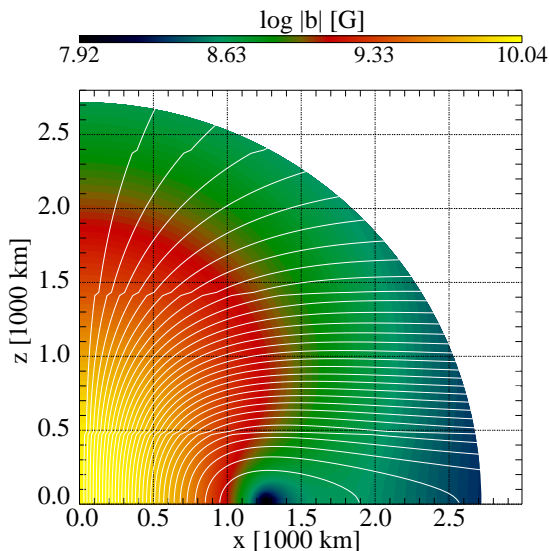


Fig. 1. Initial (pre-collapse) field configuration of model s15-B10: field strength (colour scale) and field lines. For simplicity, only one quadrant is shown.

SASI. Hence, we deem the influence of such an artificial choice for the initial field on our results only a minor one.

The field is the same as the one used by Suwa et al. (2007), defined by a vector potential of the form

$$A^\phi = \frac{b_0}{2} \frac{r_0^3}{r^3 + r_0^3} r \sin \theta. \quad (9)$$

We set the normalisation radius r_0 denoting the location of the dipole to $r_0 = 1000$ km and vary the parameter b_0 setting the field at the centre of the core between 10^{10} and 10^{12} G, i.e., in a range somewhat above that found by (Heger et al. 2005) for rotating progenitors. See Fig. 1 for a visualisation of the initial field of model s15-B10.

Tab. 2 list important parameters of our models: apart from the initial field strength, b_0 , we present time averages (over $t \in [280 \text{ ms}, 300 \text{ ms}]$) of the mean field strength in the PNS at densities above $10^{14} \text{ g cm}^{-3}$, in the convection zone inside the PNS (b_{cnv}), in the stable layer surrounding the PNS (b_{stb}), and in the gain region where neutrinos deposit energy behind the SN shock (b_{gain}). Moreover, time-averaged (over $t \in [280 \text{ ms}, 300 \text{ ms}]$) ratios of magnetic energy to internal energy and to kinetic energy in the same regions, β^i and β^k , respectively, are listed. We will define these regions more quantitatively in Sect. 4.1.

4. Results

4.1. A non-magnetised reference model

The model with $b_0 = 0$, model s15-B0, serves as a reference case to which we can compare the magnetised models; furthermore, it allows us to compare our results with previous results for similar cores. The evolution of the mean entropy profile and of the root-mean-squared lateral velocity of the model as function of time is shown in Fig. 2.

Core bounce occurs after 168 milliseconds of collapse; the shock forms at a mass coordinate of $M_{\text{sh}} \approx 0.45 M_\odot$ and starts propagating outwards. A strong negative gradient of the electron fraction triggers prompt PNS convection in a layer between an inner radius of about 15 and an outer radius that is initially at about 50 km and decreases to about 40 km at the end of the simulation. In Fig. 2, we show the upper boundary of the PNS convection zone by a solid black line. Convective velocities inside the PNS reach maximum values of $\approx 5 \times 10^8 \text{ cm s}^{-1}$ and angle-averaged r.m.s. values of $\approx 2.5 \times 10^8 \text{ cm s}^{-1}$.

After roughly 50 ms post-bounce, the shock starts to oscillate as the standing accretion shock instability (SASI Blondin et al. 2003) develops in the post-shock region. Perturbations created at the shock wave are advected with the flow towards the PNS, leading to the parallel alignment of the patterns of lateral velocity and of the (grey) mass-shell lines in Fig. 2. From these perturbations, the SASI develops in the post-shock region. Typical transverse velocities associated with the SASI reach values about 3 times as large as the convective velocities deeper inside the PNS. With increasing time, the SASI begins, starting in the immediate post-shock region, to affect a larger fraction of the post-bounce volume, until at $t \gtrsim 100$ ms the PNS convection zone is separated from the SASI region by a thin stable layer located roughly between densities of 10^{11} and $10^{12} \text{ g cm}^{-3}$. The border between the stable layer and the SASI region is shown in Fig. 2 by a solid black line.

For later reference, we list the definitions we use for the four distinct regions of the core and their respective boundaries:

1. The *inner hydrodynamically stable PNS* extends from the origin to roughly the radius where the density of the gas drops below $10^{14} \text{ g cm}^{-3}$.
2. This inner core is surrounded by the *PNS convection zone*, characterised by a negative gradient of the electron fraction. The outer boundary of this layer is associated with the location of the minimum of the Y_e profile.
3. A *stable layer* surrounds the PNS convection zone and separates the latter from the
4. *gain region* where hot-bubble convection and the SASI operate. The boundary between the stable and the gain layer is approximately given by the gain radius that defines the transition from neutrino cooling below to neutrino heating above.

Despite growing SASI activity and increasing entropy in the post-shock region and despite a slowly growing radius of the stalled shock, no explosion takes place until 550 ms after bounce. This is in agreement with simulations for $15 M_\odot$ stars (but different progenitor models) by Marek & Janka (2009) and Burrows et al. (2006).

4.2. Models with weak initial fields

Models s15-B10 and s15-B11 ($b_0 = 10^{10,11}$ G, respectively) exhibit very similar dynamics compared both to each other and to the non-magnetised reference model. The structure of the core is during several hundred milliseconds of post-bounce evolution the same as that of model s15-B0: a convective layer inside the proto-neutron star at $\rho \gtrsim 10^{12} \text{ g cm}^{-3}$ and a SASI region, separated by a thin stable deceleration layer; hence, the profiles of entropy and v_θ are in qualitative agreement with the ones shown in Fig. 2.

We discuss the evolution of the magnetic field of model s15-B10 in the following. A space-time diagram of the model

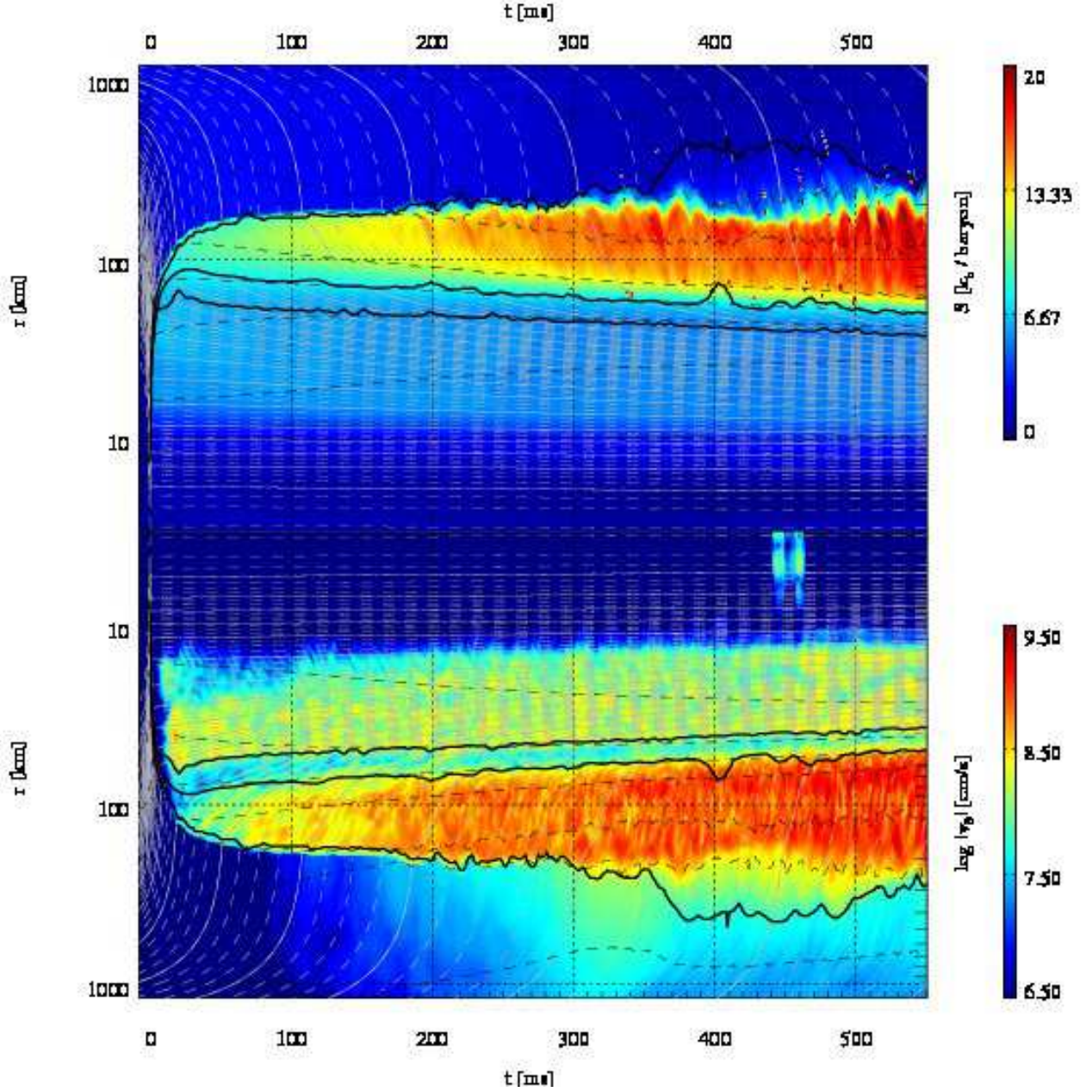


Fig. 2. Summary of the evolution of model s15-B0. The upper and lower panels show angular averages of the entropy per baryon and the of root-mean-square of the lateral velocity, respectively (colour coding) as a function of radius and post-bounce time. The grey lines indicate the positions of different mass shells; the intervals between solid and dashed lines are 0.1 and 0.025 solar masses, respectively. The thick black lines show (from small to large radii) the outer boundaries of the PNS convection zone and of the stable layer beneath the SASI region and the outermost position of the shock wave. The thin dashed black lines depict iso-density surfaces of 10^n g cm^{-3} , $n = 14, 13, \dots$

(Fig. 3) shows angular averages of the current density¹ $j = (\nabla \times \mathbf{b})^\phi$ and the field strength. We use the current density to detect spatial variations of the magnetic field. While not all patterns of j are necessarily caused by Alfvén waves, Alfvén waves are associated with a non-zero current density. Hence, we can try to identify these waves in the current distribution.

Without changing the field geometry, compression amplifies the magnetic field during collapse along with the maximum den-

sity as $\rho_{\text{max}}^{2/3}$, leading to a gain of a factor of ≈ 500 and ≈ 25 in the maximum field strength and total magnetic energy, respectively.

Further amplification occurs in the PNS convection zone (see Fig. 4). Within roughly 10 ms after the onset of PNS convection, the mean field is amplified by a factor of ~ 3 between radii of ~ 20 and ~ 60 km. Field growth is driven by the convective overturn motions of the gas (indicated in the deviations of Y_e from its angular mean value, see *right half* of Fig. 4) and leads to a filamentary field topology (same figure, *left half*). This strongly non-uniform structure is reflected in the large fluctuations of the current density visible in the top panel of Fig. 3 (first ~ 100 ms

¹ For simplicity, we omit the factor $\frac{4\pi}{c}$ in the definition of the current density and consider only the ϕ -component, neglecting the vanishing components j^r and j^θ .

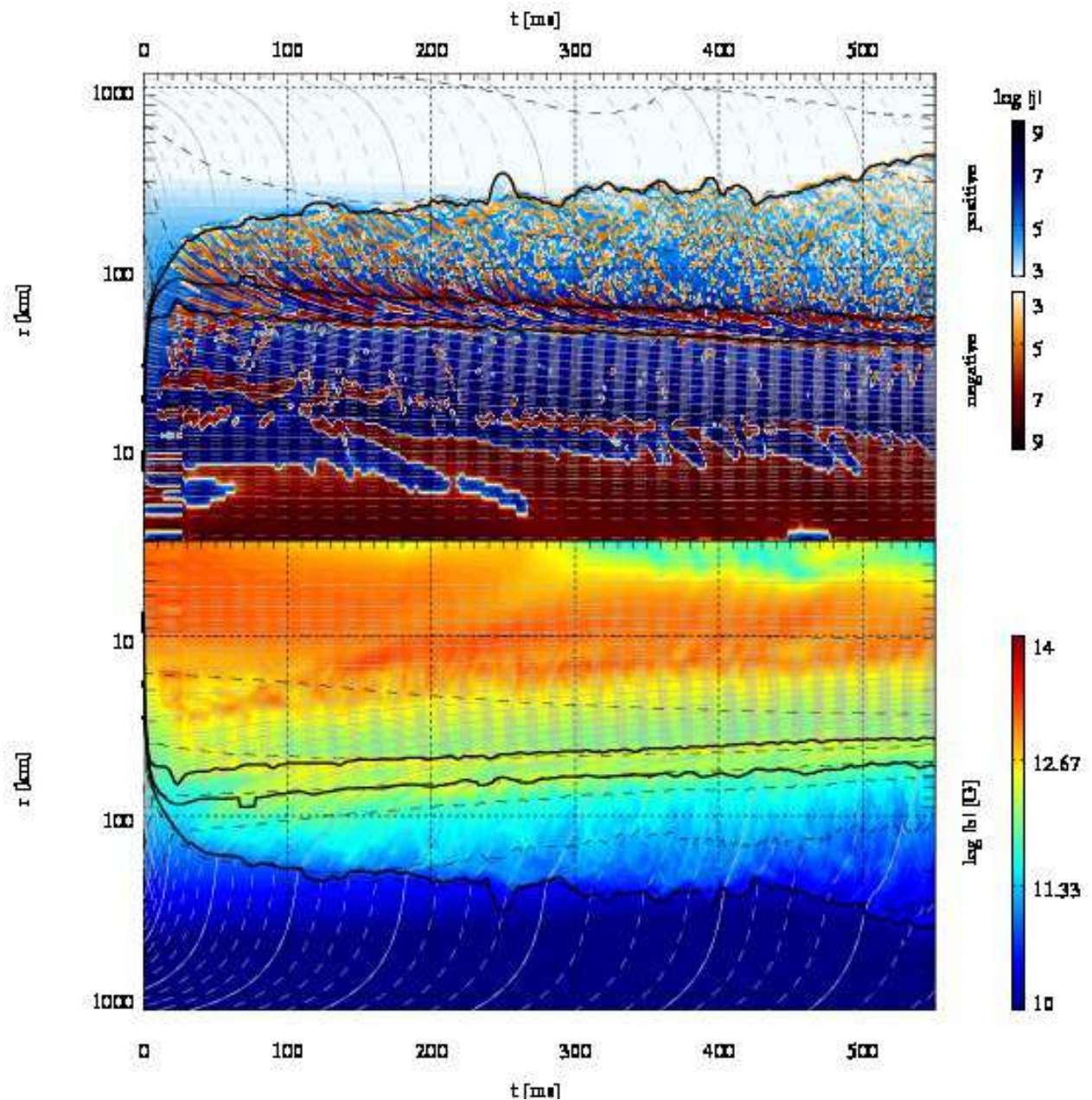


Fig. 3. Evolution of model s15-B10. The panels show in colour coding the logarithm of the lateral average of the current density (*top panel*; the intensity of the colour encodes the absolute value and the blue and red colours distinguish between positive and negative signs) and the logarithm of the mean magnetic field strength (*bottom panel*). The lines have the same meaning as in Fig. 2.

at radii between ~ 15 and ~ 60 km). After about 100 ms, the amplitude of variations of the current density in the convective layer decreases. While j still varies on short temporal and spatial scales, larger coherent fluctuations are mostly absent during this phase: compare the larger red ($j^\phi < 0$) patches in the PNS convection zone at $t \lesssim 100$ ms to the convection zone at later times standing out as a broad blue ($j^\phi > 0$) band with little contribution of negative currents. In this phase, the angular average of the current density in the PNS convection zone is very regular and shows little temporal variation. It is dominated by one large-scale pattern, viz. columns of strong magnetic field generated by flows converging at the axis due to the constraint of axisymmetry (Fig. 4). These very persistent features are associated with a strong positive current density whose value is dominating what-

ever fluctuations there may be due to convective cells at the same radii.

As soon as the SASI develops, we find appreciable lateral velocities also in the region above the PNS convection zone. An early stage of the development of the SASI can be seen already in the Y_e variation close to the shock in Fig. 4: small deformations of the shock excite perturbations advected inwards. These perturbations are associated with kinks in the magnetic field lines. Geometrically, they take the form of sheets oriented parallel to the shock, i.e., roughly at constant radius, containing a magnetic field with a strong θ -component. This translates into a non-zero derivative $\partial_r b^\theta$, i.e., a non-zero current density. Consequently, the perturbations can be identified easily in the top panel of Fig. 3 as the alternating blue and red bands starting at the shock and

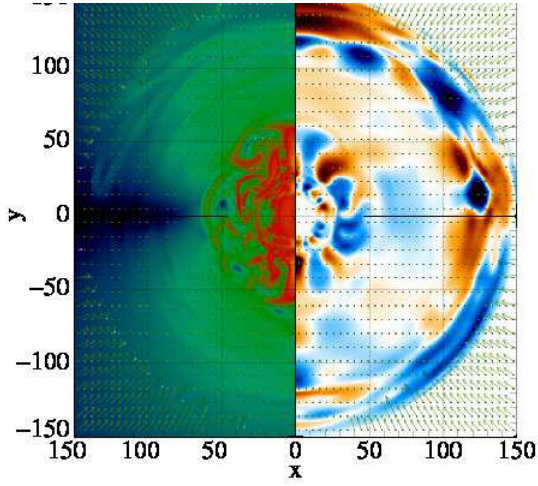


Fig. 4. Snapshot of model s15-B10 shortly after the onset of PNS convection at $r \lesssim 50$ km. The *left* and *right* panels show the logarithm of the magnetic field strength and the deviation of the electron fraction from its angular average. Vectors indicate the velocity field.

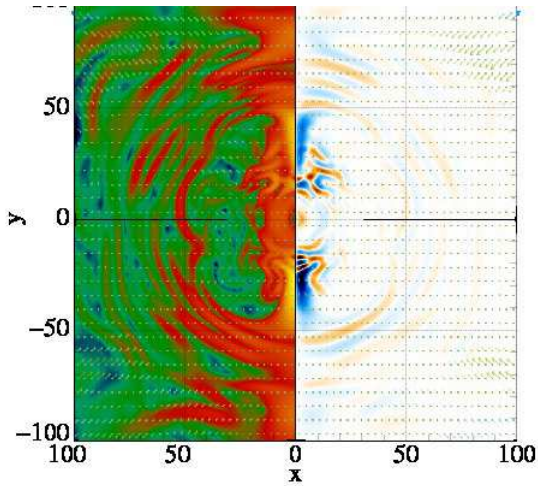


Fig. 5. Snapshot of model s15-B10 at $t \approx 120$ ms post-bounce. The panels show, apart from the velocity field, the logarithm of the magnetic field strength (*left*) and the current density (*right*).

falling towards the deceleration layer. Propagating at the velocity of fluid accretion, these bands are parallel to the mass shells (grey lines).

When the accretion flow decelerates above the PNS convection zone, these sheets pile up at the deceleration layer (cf. Fig. 5 at $r \gtrsim 50$ km), leading to a local increase of the magnetic energy. The bottom panel of Fig. 3 indicates that this process happens throughout the entire evolution and magnetic energy continues to accumulate.

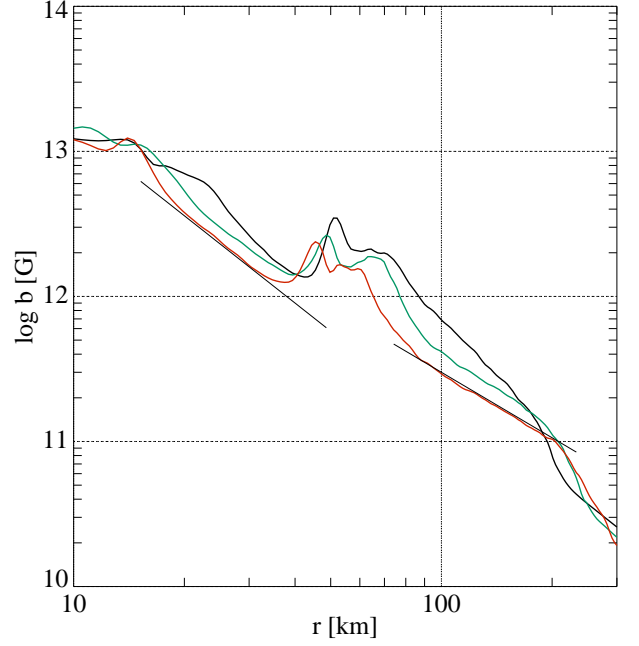


Fig. 6. Average radial profiles of the field strength of model s15-B10 in the post-bounce phase (time averages over $t \in [100;200]$ ms (black), $t \in [200;300]$ ms (green), $t \in [300;400]$ ms (red) post-bounce). The thin straight lines show profiles $\propto r^{-2}$ ($r < 50$ km) and $\propto r^{-3/2}$ ($r > 80$ km).

4.2.1. Sub- and superalfvénic regions

In the following, we discuss the propagation of MHD waves in the core. We will not touch upon fast modes and focus only on slow and Alfvén waves. Whereas Alfvén and slow modes propagating across the field lines are clearly distinct solutions (they have, e.g., different polarisation states and different propagation speeds), they degenerate when propagating along the field lines. In this case, they have identical propagation speeds, viz. the Alfvén speed. Because we expect the dynamics to be dominated by the modes propagating fastest, i.e., the ones travelling (anti-)parallel to the field lines, we will consider these modes only. Because of the degeneracy of slow and Alfvén modes in such a case, we will refer to these modes as Alfvén waves for short, postponing an investigation of the possible differences between the two classes of modes. It is expected (J. Guilet, *private communication*) that slow modes behave very similarly to Alfvén waves.

An essential requisite for this evolution is that the flow is superalfvénic, i.e., the flow velocity is larger than the Alfvén velocity of the magnetic field

$$c_A = \frac{\sqrt{b^2}}{\sqrt{\rho}} = 10^6 \text{ cm s}^{-1} \left(\frac{|b|}{10^{12} \text{ G}} \right) \left(\frac{10^{12} \text{ g cm}^{-3}}{\rho} \right)^{1/2}. \quad (10)$$

A magnetic field \mathbf{b} allows for the propagation of Alfvén waves in and against the direction of the field at the same propagation speed, c_A relative to the flow of the gas carrying the magnetic field, i.e., with a velocity $\pm \mathbf{c}_A = \pm \mathbf{b}/|b| c_A$. The total velocity of such a pair of waves in the lab frame, where the gas moves with a velocity \mathbf{v} , is $\mathbf{v} \pm \mathbf{c}_A$. Hence, an Alfvén point develops where the component of the Alfvén speed directed along the fluid velocity has the same absolute value as \mathbf{v} . At that point, one of the pair of Alfvén waves, viz. the one with an Alfvén velocity antiparallel

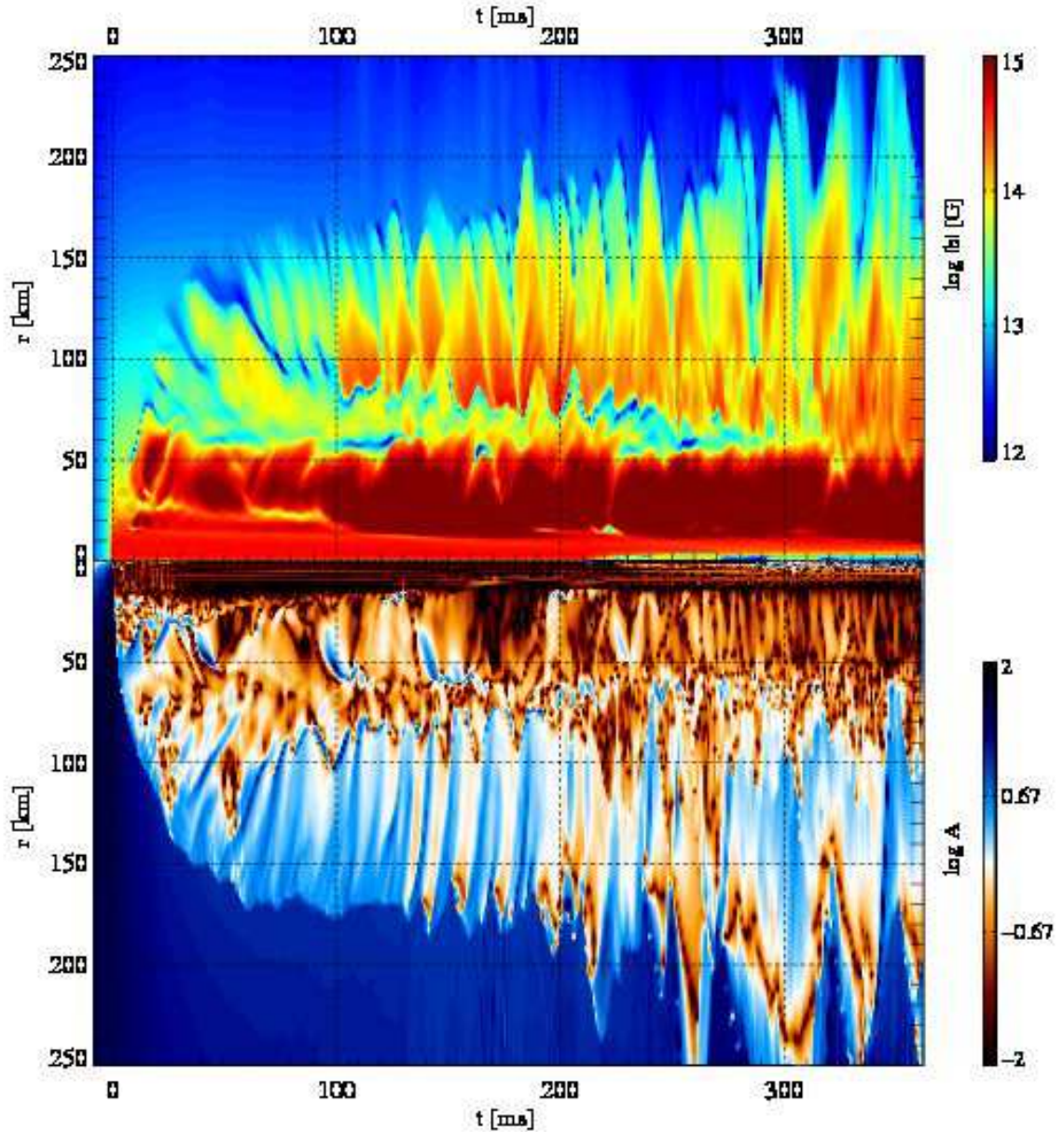


Fig. 7. Space-time diagram of the magnetic field strength (*top panel*) and the logarithm of the Alfvén number (*bottom panel*) of model s15-B11.5 along the north pole.

to \mathbf{v} , is trapped, i.e., has vanishing total velocity, while the other one passes the Alfvén point at a total speed $2|\mathbf{v}|$.

To quantify the importance of the magnetic field, we define the total, parallel, and perpendicular Alfvén numbers,

$$A_{\text{tot}} = \frac{|\mathbf{v}|}{|c_A|}, \quad (11)$$

$$A_{\parallel} = \frac{\mathbf{v} \cdot \mathbf{c}_A}{c_A^2}, \quad (12)$$

$$A_{\perp} = \frac{|\mathbf{v} \times \mathbf{c}_A|}{c_A^2}. \quad (13)$$

While A_{tot} compares kinetic and magnetic energies directly, A_{\parallel} and A_{\perp} measure two effects important to Alfvén waves propagating along the field:

- A_{\parallel} regulates the total (lab-frame) propagation speed of the wave, composed of the (comoving) Alfvén velocity and the flow speed, $\pm c_A + \mathbf{v}$; $|A_{\parallel}| = 1$ indicates an Alfvén point where the waves stall.
- A_{\perp} is a parameter relevant to the excitation of perturbations orthogonal to the magnetic field, comparing the velocity displacing magnetic field lines with the tension of the field lines. Alfvén waves rely on magnetic tension as restoring force; hence, their excitation occurs for $A_{\perp} < 1$; otherwise, the field can be distorted (e.g., amplified in a stretch-twist-fold dynamo), but the distortions are beyond the linear regime of Alfvén waves.

The gas flows triggered by PNS convection as well as by the SASI are highly superalfvénic. Though there is, in principle, a small stable region between the convection and the SASI

regions, where the accretion is decelerated and only small lateral velocities are present, the flow in this region remains superalfvénic because of overshooting from the PNS convection and the SASI regions. Travelling along a field line connecting the convection zone with the SASI region, one observes a drop of all three Alfvén numbers in the deceleration region, but they still remain considerably above unity. Hence, there is neither any significant excitation of Alfvén waves nor is there an Alfvén point where amplification as proposed by Guilet et al. (2010) could happen. Magnetic perturbations are unable to travel upwards against the accretion flow; furthermore, the relative weakness of the field prohibits dynamic back-reaction. Thus, this is a purely kinematic effect.

The combination of these effects leads to the time evolution of the average field profile shown in Fig. 6. Across the PNS convection zone, the average field strength drops by an order of magnitude. At its upper boundary, the pile-up of field accreted from the outer layers leads to a strong local increase of the field strength, while in the SASI region, the radial decrease of the field continues following a slightly flatter law ($b \propto r^{-3/2}$) than in the PNS convection zone ($b \propto r^{-2}$). The steepening of the slope at $r \sim 200$ km marks the minimum radius of the shock wave.

For model s15-B10, the flow is superalfvénic almost everywhere. Sizeable subalfvénic regions develop only for significantly stronger fields. The convective flows of model s15-B11.5, with an initial field strength given by $b_0 = 10^{11.5}$ G $\approx 3.16 \times 10^{11}$ G, are only moderately superalfvénic. In particular, along the pole, where the magnetic field is enhanced artificially for symmetry reasons, the Alfvén numbers are below unity (Fig. 7). The thin layer separating PNS convection and hot bubble consists of both sub- and superalfvénic regions, while the accretion flow is mostly superalfvénic.

In analogy to the model discussed above, perturbations of the magnetic field created at the shock wave are advected towards the PNS. The field piling up above the PNS, dominated by a strong lateral component generated by the complex overturns of the gas flow, forms shells around the PNS. Since the radial component is weak, Alfvén waves are bound to travel at roughly constant radius. Consequently, the location of an Alfvén point along a field line is determined not by the radial flow alone but mostly by the lateral velocity. Whereas the former tends to go through zero in the deceleration region, the latter can, in principle, have a stochastic and chaotic behaviour and dynamical evolution.

Thus, while there may be Alfvén points in this region, their location is highly variable; they may even, depending on the flow, cease to exist for a certain time when the flow becomes superalfvénic or subalfvénic in the entire region. This may have adverse effects on the efficiency of the amplification process proposed by Guilet et al. (2010). Despite the stochastic nature of these variations, we find a systematic trend: the stronger the magnetic field is, the farther out stretches the layer of accumulated magnetic field on average. Since this layer corresponds to the hydrodynamically stable region between PNS convection and the SASI region, the trend of a growing radius of the region where the field accumulates can be seen most easily in the average profiles of the lateral velocity shown in Fig. 8. This effect is an, albeit small, indication of dynamic back-reaction of the field onto the flow.

4.2.2. Accretion columns

The accretion columns display much stronger radial components of the field and the velocity, while non-radial fields of a considerable strength may be present in the flux sheets surrounding them.

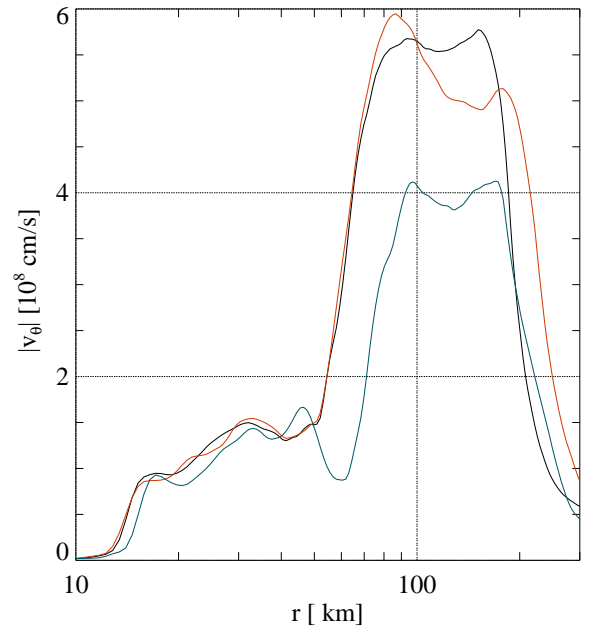


Fig. 8. Root-mean-square averages of the θ -component of the velocity as a function of radius for models s15-B10 (black), s15-B11 (red), and s15-B11.5 (blue). Time averages over several tens of milliseconds in the late post-bounce phase (at $t \approx 300$ ms) are shown.

Accretion proceeds mostly through a narrow stream at the poles, and mass conservation leads to an increase of the flow speed as the gas is accreted through a small solid angle rather than uniformly over all angles. Eventually, the flow reaches sound speed. Analogously, flux conservation increases the magnetic field strength in the accretion funnels. Depending on the initial field strength, the Alfvén number of the accretion flow and $\beta = P/P_{\text{mag}}$ may be of order unity or much greater.

Due to the high Mach number, pressure perturbations of the accretion flow may steepen, in some cases yielding discontinuities. In particular, weak shock waves may mark the lower end of the column, providing a very abrupt deceleration of the gas. Due to the dissipation of kinetic into internal energy, the entropy of the matter above the shock is higher than that of the gas in the deceleration and PNS convection layers where S is nearly uniform.

In the presence of a magnetic field, these features are not purely hydrodynamic but rather MHD structures associated with a bending of the field lines, i.e. a current density: the field, predominantly radial in the accretion column, is folded by the relatively high lateral velocity in the deceleration region and is mostly lateral in this layer. This effect is weakest in the polar accretion funnels because the axial symmetry restricts the development of a non-radial field considerably. In all accretion columns, both velocity and magnetic field are dominated by their respective radial components; for the polar accretion flow, this dominance of the radial components holds even at radii below the lower end of the accretion stream, i.e., for $r \lesssim 70 - 100$ km. Accretion streams at intermediate latitudes tend to punch into gas threaded by strong lateral field lines and moving at considerable speed along constant radius.

For a sufficiently strong magnetic field, an Alfvén point may be located in the accretion stream; for a steep gradient of v_r , or

even a discontinuity at the lower end of the stream, this is a most natural place for the Alfvén point.

Conditions are most favourable for the formation of a stable Alfvén point in radial polar accretion streams. We show the time evolution of the magnetic field and the Alfvén number along the north pole of model s15-B11.5 in Fig. 7. Initially, accretion is roughly spherical, but after $t \approx 80$ ms, polar accretion streams begin to form; as a consequence, the radial velocity behind the shock increases abruptly. This stream remains active for the rest of the simulation. It is, however, subject to strong fluctuations on time scales of about 10 milliseconds. These oscillations affect the outer and inner termination radius of the accretion flow, the velocity, and the magnetic field. They are caused by lateral motions due to convection and the SASI in the surrounding gas that lead to an episodically varying cross section of the funnel. Following the variations of the accretion velocity, the Mach number of the flow oscillates around unity. For this model, the same holds for the Alfvén number.

The accretion flow terminates in a steep gradient hosting an Alfvén point. This point is first, at $t \approx 100$ ms post-bounce, situated at a radius of 80 kilometres, i.e., about 30 kilometres above the PNS convection layer; later it retreats to lower radii as the core contracts. The intermediate layer between the termination point of the accretion column and the PNS convection layer is, though threaded by a weaker magnetic field, filled by gas at subalfvénic velocities. Hence, at these radii, Alfvén waves could propagate from below towards the accretion flow. Given a typical Alfvén velocity in this layer of $c_A \sim 2 \times 10^8 \text{ cm s}^{-1} (b_0/10^{11} \text{ G})$, they should traverse the intermediate layer within $\tau_A \sim 10 \text{ ms}/(b_0/10^{11} \text{ G})$, i.e., on the time scale of the oscillations of the accretion column. This has two consequences: first, it complicates the identification of Alfvén waves, and, second, it may limit the applicability of the scenario of amplification of Alfvén waves in this context.

The fluctuations of the accretion velocity and the position (radius, possibly also latitude) of the termination point of the accretion column induce perturbations propagating in the layer between the accretion column and the PNS convection region, i.e., outside a radius of about 50 kilometres and inside a radius that recedes gradually from about 80 – 100 kilometres at $t \approx 100$ ms to roughly 60 km at $t \approx 300$ ms. Partially, these perturbations can be entrained in matter flowing upwards and thus sustaining the magnetic field in the hot-bubble region. Additionally, overshoot from the convective layer below contributes to a certain degree to maintaining the turbulence in the deceleration region.

4.2.3. Field amplification

Though, in principle, the dynamics in this layer can be expressed in terms of basic MHD waves, it is not trivial to identify these simple solutions in the highly variable fields, preventing deeper insights into the field amplification mechanisms. Therefore, we must try to find indirect evidence for the amplification processes at work. To this end, we distinguish between kinematic and dynamic amplification, i.e., processes that do not depend on the seed magnetic field (at least during an initial phase when it is still sufficiently weak) and processes for which the amplification is some function of the seed field, respectively.

Convection and the SASI amplify the field kinematically. Hence, they should amplify the field by a given factor independent of the seed field. This is demonstrated by the comparison of space-time averages of radial profiles of the magnetic field strength of models with different initial fields shown in Fig. 9. Corrected for the scaling with the initial field strength, the pro-

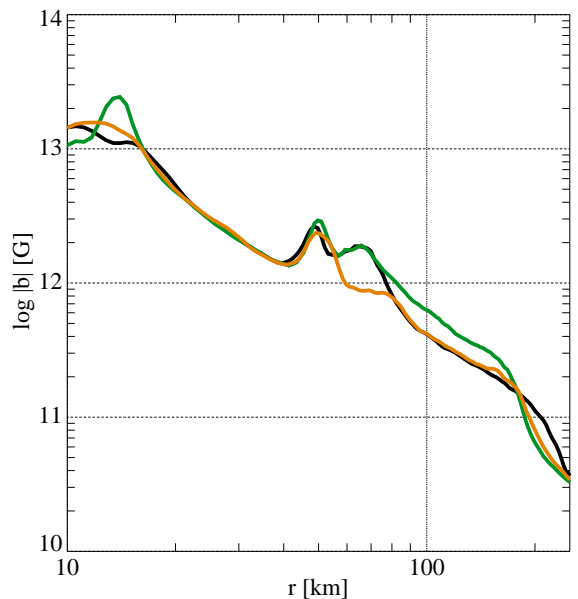


Fig. 9. Space-time averages of the magnetic field strength of models s15-B10 (black), s15-B11 (green), and s15-B11.5 (orange line). We average over times between $t = 200$ ms and $t = 300$ ms post-bounce. The fields of models s15-B11 and s15-B11.5 are scaled according to their initial strength.

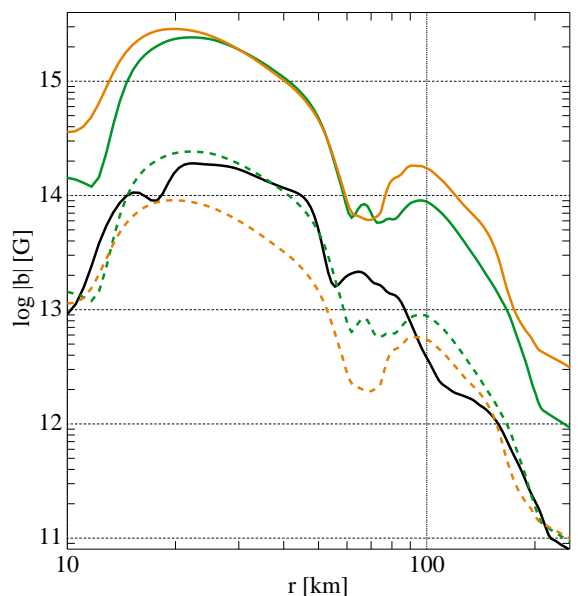


Fig. 10. *Left panel:* Temporally averaged (over post-bounce times of $120 \text{ ms} \lesssim t \lesssim 200 \text{ ms}$) radial profiles of the magnetic field strength along the north pole for models s15-B10 (black), s15-B11 (green), s15-B11.5 (orange). The field strength is represented by solid lines; the dashed lines show the field strength scaled by the ratio of initial field strength.

files of all three models are remarkably similar. The main differences appear in the deceleration region, where neither the radial collapse nor convection or the SASI are the main amplification mechanisms.

The Alfvén mechanism due to Guilet et al. (2010), on the other hand, depends on the presence and the location of

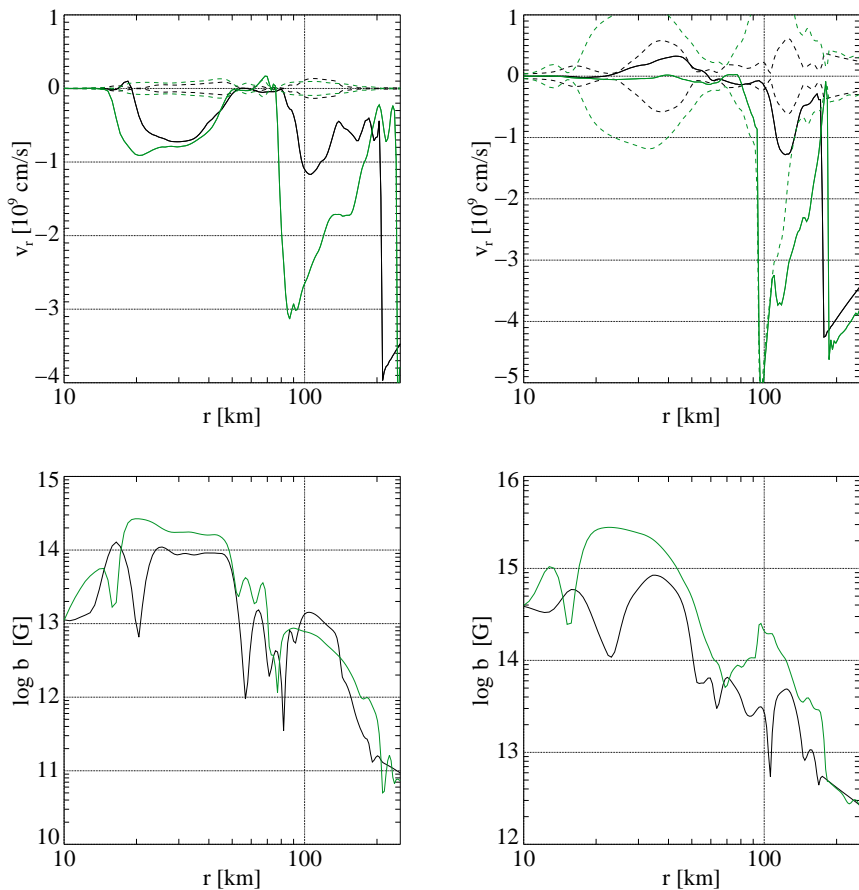


Fig. 11. The *top panels* show profiles of the radial velocity (solid lines) along the north pole of models s15-B10 (*left*) and s15-B11.5 (*right*); the dashed lines show the Alfvén velocity, c_A , and its negative, $-c_A$. The *bottom panels* depict profiles of the magnetic field strength of the same models. In all panels, black and green lines denote the profiles at $t \approx 100$ ms and $t \approx 200$ ms post bounce, respectively.

Alfvén points, hence on the initial field strength. Furthermore, the Alfvén-wave mechanism should be most efficient along the polar axis (as discussed above and shown in Fig. 7). A comparison of the polar regions of models with different initial field strengths should therefore allow us to determine the importance of the Alfvén-wave mechanism.

We compare time averages of the field strength along the north pole for different initial fields in Fig. 10 and profiles for two times in Fig. 11. In the PNS convection zone, the field is amplified roughly by the same factor irrespective of b_0 , but only until it reaches kinetic equipartition. This limit is reached by model s15-B11.5. The field decreases with radius in the convection zone and it exhibits a further drop by about an order of magnitude at the upper boundary of the convective layer inside the PNS.

After a few tens of milliseconds, the evolution of models s15-B10 and s15-B11.5 diverges. The weak-field model shows a coherent stable downflow inside the convection region (at radii between 20 and 50 kilometres) and a rather smooth velocity profile in the surrounding layers (at radii above 70 kilometres; see the black line in the *upper left panel* of Fig. 11). Alfvén points may be located at the border between the PNS convection region and the accretion flow. The accretion flow transports the magnetic field towards the convection zone and establishes a temporally averaged profile varying around $|\mathbf{v}| \propto r^{-3}$ between the convection zone and the shock wave.

In model s15-B11.5 (for profiles at different times, see the *right panels* of Fig. 11), strong perturbations originating in the convection zone propagate upwards against the accretion flow (note the large positive velocity below $r \approx 50$ km). Under the influence of perturbations converging from below and above,

the lower end of the accretion column develops an increasingly steep profile until a discontinuity is formed a few tens of kilometres above the PNS convection zone (visible in the green line at $r \approx 100$ km; the discontinuity located at $r \approx 200$ km is the stalled supernova shock wave). Magnetic energy is transported towards this point from both sides (some of the accreted field can be identified in the black curve in the *lower right panel* above $r \approx 100$ km) and a region of enhanced field correlated with the termination of the accretion flow is created, visible right at the discontinuity (at $r \geq 90$ km in the green line).

Thus, upflows travelling from the PNS convection zone towards the polar accretion columns play a role in stopping the accretion flow and shaping the radial profile at its lower end. We find that the lower end of the equatorial accretion column develops steeper profiles, too, but this is caused by a different effect: the accretion flow continues to smaller radii until it is terminated at a radius of $r \approx 60$ km, i.e., it terminates when it hits the high-density layer near the outer boundary of the PNS convection zone. These discontinuities do typically not coincide with an Alfvén point and are not associated with an enhancement of the magnetic energy.

Hence, we find that field amplification, while dominated by kinematic effects such as convection and the SASI, has also a certain contribution from the growth of the field by the superposition of perturbations propagating in opposite directions between the regions of PNS convection and the SASI.

4.3. Stronger magnetic fields

For an initial field of $b_0 = 10^{12}$ G (model s15-B12), we find, much like in the models with weaker fields, a convection layer

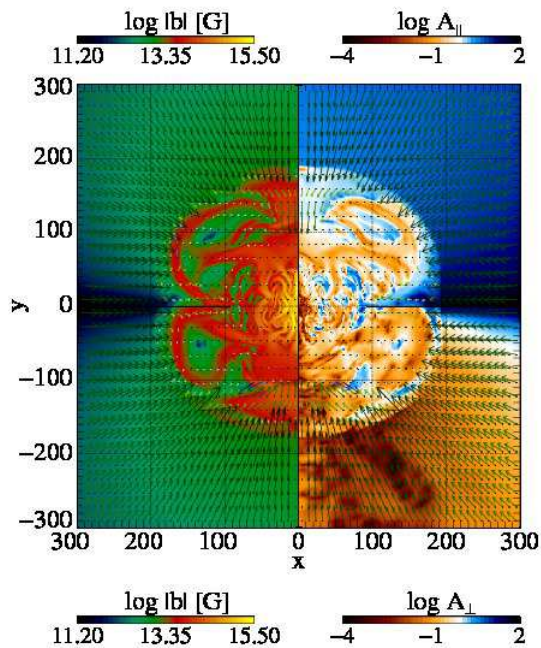


Fig. 12. Snapshot of model s15-B12 at $t \sim 130$ ms post-bounce. The hot-bubble region is dominated by a super-equipartition (w.r.t. the velocity) magnetic field; this is particularly evident in the large-scale arcs of the magnetic field right behind the shock wave. In these arcs, which separate gas of a high entropy on the inside from low-entropy gas on the outside, the magnetic field reaches equipartition with the internal energy of the gas. Gas falling through the shock wave is deflected sideways towards two polar and an equatorial accretion column, yielding a quadrupolar structure of the flow and the magnetic field, in contrast to models with weaker fields, where the flow structures are dominated by higher multipolarity.

inside the PNS and, outside of the PNS, the hot-bubble region dominated by the SASI. Due to the much stronger initial field, however, the accretion flow onto the PNS is subalfvénic almost out to the shock wave.

The spatial structure of the model at $t \approx 130$ ms is displayed in Fig. 12. The hot-bubble region is dominated by a super-equipartition (w.r.t. the velocity) magnetic field; this is particularly evident in the large-scale arcs of the magnetic field right behind the shock wave. In these arcs, which separate gas of a high entropy on the inside from low-entropy gas on the outside, the magnetic field reaches equipartition with the internal energy of the gas. Gas falling through the shock wave is deflected sideways towards two polar and an equatorial accretion column, yielding a quadrupolar structure of the flow and the magnetic field, in contrast to models with weaker fields, where the flow structures are dominated by higher multipolarity.

Accretion proceeds along a few directions, viz. in these columns, at trans- and superalfvénic velocities, whereas the gas moves subalfvénically between these accretion flows (the blue regions in the *right half* of Fig. 12). In these regions, the Alfvén points lie far out in the accretion/SASI region at more than 150 kilometres, whereas they are located roughly at the deceleration radius in the downflows, i.e., at radii around 100 kilometres (see the borders between blue and red regions in the *right halves* of Fig. 12). While these regions exhibit some variations of their shape with time, they are present during the entire post-bounce time. It is also worth mentioning that A_{\perp} is less than unity in most of the post-shock regions, meaning that perturbations of the magnetic field can indeed be described in terms of Alfvén waves, whereas A_{\parallel} varies between values greater and less than unity, i.e., the waves are either trapped by the flow or can escape.

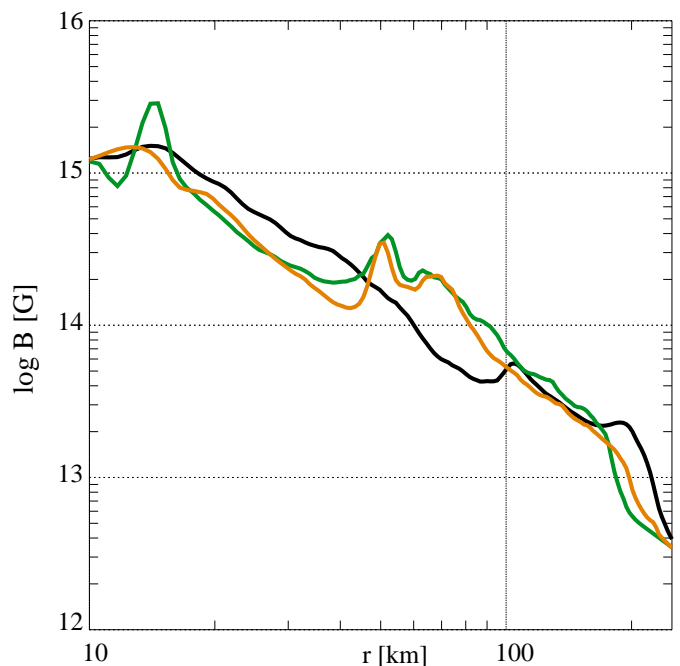


Fig. 13. Average (over angle and time, $160 \text{ ms} \lesssim t \lesssim 220 \text{ ms}$ post-bounce) profiles of the magnetic field strength of models s15-B12 (black), s15-B11 (green), and s15-B10 (orange), corrected for the scaling of the initial field strength in the case of the latter two models.

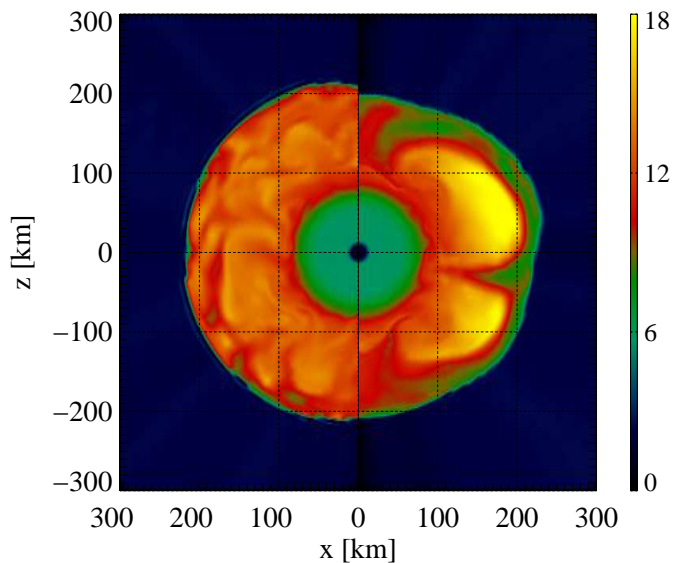


Fig. 14. Comparison of the entropy per baryon of models s15-B10 (*left half*) and s15-B12 (*right*) at $t \approx 170$ ms.

Due to the stable quadrupolar structure of the flow, the dynamics of an accretion column, as outlined in Sect. 4.2.2, is important for the evolution of this model. Magnetic field is accreted in the downflows, while it can rise against the accretion in the broad regions of slowly moving gas between. Similarly to model s15-B11.5, waves travel upwards along the polar axis from the PNS convection zone. The accretion flow is decelerated abruptly at a discontinuity at the lower end of the accretion column, and

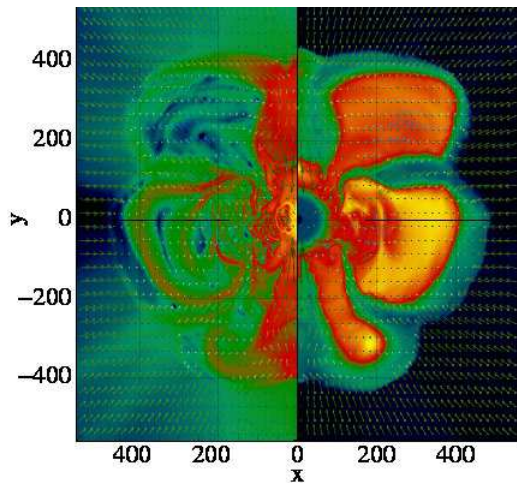


Fig. 15. Snapshot of model s15-B12 at $t \approx 300$ ms. The *left* and *right* halves shows the logarithm of the magnetic field strength and the entropy per baryon, respectively.

an Alfvén point is located there. At this point, we find a pronounced enhancement of the magnetic field.

Fig. 13 displays a comparison of average profiles of the magnetic fields for models models s15-B12, s15-B11, and s15-B10, corrected for the scaling of the initial field strength. While the models with weaker initial fields (green and orange lines) show a distinct increase of the field strength at the outer boundary of the PNS convection zone, i.e., at $r \approx 50$ km, a similar feature is present for the model with stronger field at a much larger radius of $r \sim 100$ km; in this case, the profile is described roughly by a uniform power law out to this point. The maximum field strength of model s15-B12 is of the order of 10^{15} G at the base of the convection zone.

Between the accretion columns, strong magnetic flux sheets are located at the lateral and upper boundaries of the upwards flowing plumes. This is visible, e.g., in the large arcs of field connecting the accretion columns immediately behind the shock (see Fig. 12). Gas and magnetic field accreted in the accretion columns rises in these regions from the deceleration layer. On the other hand, rising magnetic flux can, upon reaching the boundaries of the plumes, be entrained in the accretion flow and thus increase the accreted magnetic energy.

In Fig. 14, we compare the entropy distribution of models s15-B10 (*left half* of the figure) and s15-B12 (*right half*) at $t \approx 170$ ms. The stable downflows of the latter model transport matter of low entropy towards the PNS where it is gains energy by neutrino heating. In this model, heating leads to a higher entropy of the gas rising between the accretion columns than in model s15-B10. This is caused by a magnetic confinement of the bubble at small radii and thus a longer exposure of the gas to strong neutrino heating.

The shock expands gradually until $t \approx 340$ ms when it reaches an outermost location of about $r \approx 600$ km. We show a snapshot of the model shortly before maximum shock expansion in Fig. 15 and a space-time diagram of the model in Fig. 16. At maximum expansion, the quadrupolar structure is replaced by more complex flows. The model exhibits a large-scale pattern of low-order multipoles. Then, expansion ceases and the shock re-

tracts again to $r \sim 300$ km, but it starts to expand again after $t \approx 420$ ms. At the end of the simulation, $t \approx 500$ ms, its maximum radius is 600 km again. While large fluctuations of the shock radius can be found in other models as well, this model is characterised by a clearly stronger expansion. The shock shows appreciable deformations; however, we do not find a very large global asphericity. The axis ratio is around unity during the late phases of the simulation. This can be seen, e.g., in the space-time diagram in Fig. 16: the regions of essentially high values of the angular averaged entropy and magnetic field extend out to the maximum shock radius. In a model with a strongly deformed shock, the maximum shock radius can be considerably larger than the radius out to which these variables assume high values.

4.4. Comparison of global quantities of our models

After the discussion of the magnetic-field amplification and of the structural differences of the simulated models in the previous sections, we conclude the presentation of our results by a comparison of important global quantities characterising the overall evolution of our models.

We evaluate the total mass and the kinetic and magnetic energies contained in the gain region, i.e., in the region between the shock wave and the stable layer surrounding the PNS. In this region, the matter gains energy by reactions with neutrinos diffusing out of the PNS, and hot-bubble convection and the SASI operate.

The mass in the gain region, m_{gain} (shown for the non-magnetic model s15-B0, one weak-field model (s15-B11), and the strong-field model s15-B12 in the *left panel* of Fig. 17), increases during the first 50 milliseconds post-bounce and peaks at about $0.055M_{\odot}$ for all models. Afterwards, the mass decreases gradually, falling below $0.02M_{\odot}$ after $t \sim 320$ ms, in all but the strongest magnetised model. In the case of model s15-B12 m_{gain} instead levels off at a value of $m_{\text{gain}} \approx 0.04M_{\odot}$. This different behaviour reflects the different evolution of the shock wave. While the outermost shock position can reach a radius of ~ 500 km along the poles, the average shock radius oscillates around a value of $r_{\text{shock}} \gtrsim 200$ km in the non-magnetised and the weak-field models. On the other hand, the shock expands to radii of 300 – 500 km at all latitudes in the strong-field model. Hence, a higher mass can be affected by neutrino heating in the model with the strongest initial field investigated. Although our models do not allow us to draw any firm conclusions on the long-term evolution of the models, we may estimate tentatively from the evolution of m_{gain} that model s15-B12 is closest to a successful explosion. Further indication of a different behaviour of weak-field and strong-field models is provided by the total energy of the matter in the gain region, i.e., the sum of internal, kinetic, magnetic, and gravitational energies. We find that this total energy of model s15-B12 exceeds that of model s15-B0 by about 5×10^{50} erg around $t = 440$ ms.

The lateral kinetic energy in the gain region, $e_{\text{kin;gain}}^{\theta}$ (shown in the *middle panel* of Fig. 17 for the same models), indicates the strength of hot-bubble convection and of the SASI. In agreement with the evolution of m_{gain} , the lateral kinetic energy of model s15-B12 exceeds that of the other models at late times ($t \gtrsim 300$ ms) by a factor of roughly 2. Apart from this difference, we find a higher value of $e_{\text{kin;gain}}^{\theta}$ in model s15-B12 than in the other models even at early times, $t \lesssim 120$ ms, when all models have a very similar mass in their gain regions. Thus, the lateral kinetic energy per unit mass, or the average lateral velocity, is

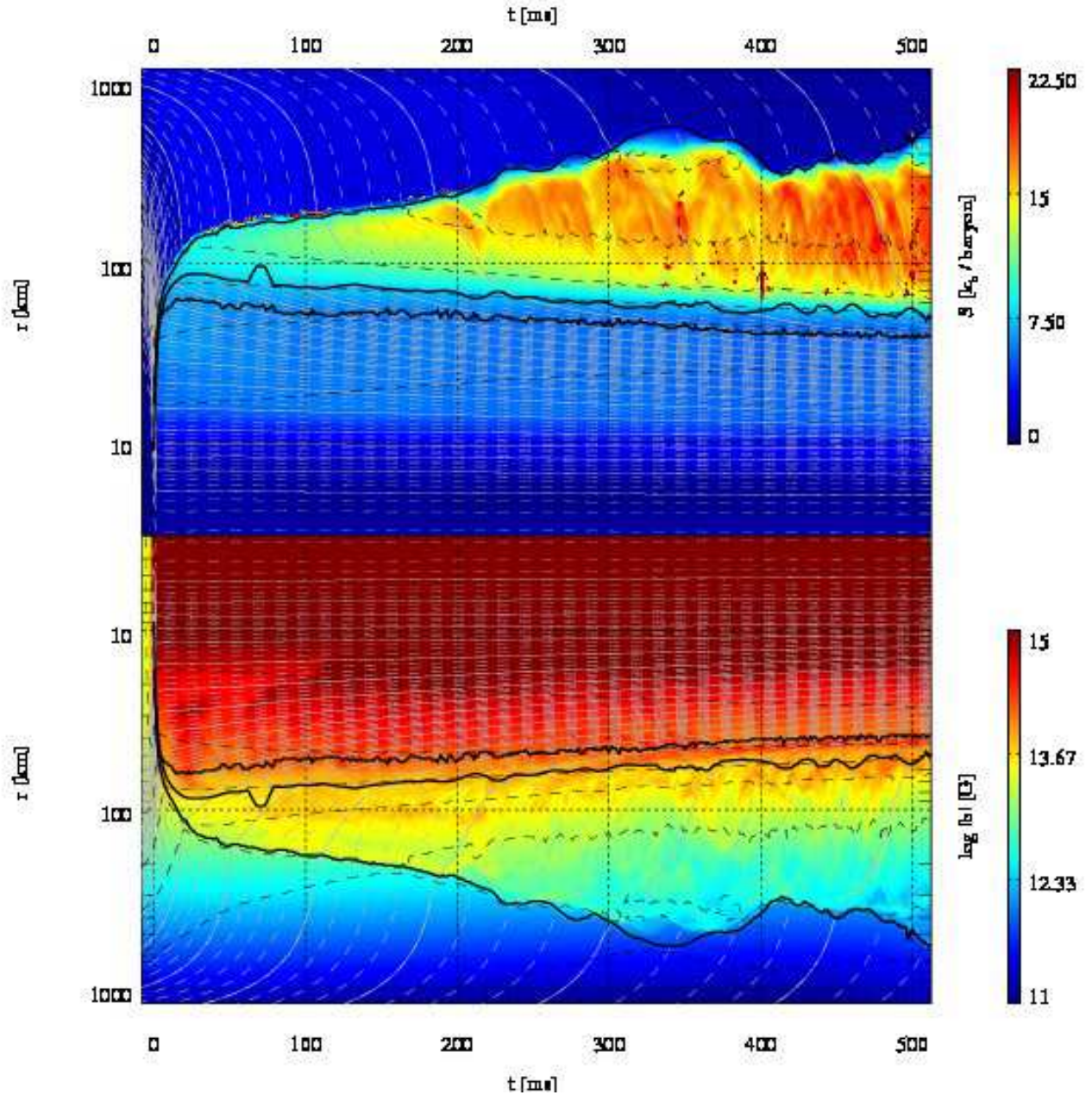


Fig. 16. Space-time diagram of model s15-B12. The top and bottom panels show colour-coded the entropy per baryon and the logarithm of the magnetic field strength, respectively. Additionally, mass shells and density contours are plotted, using the same spacing as in Fig. 2.

largest in model s15-B12. This is a consequence of the peculiar quadrupolar flow pattern developing solely in this model.

We compare the amount of field amplification in the gain regions of all magnetised models in the *right panel* of Fig. 17. For all models, an initial rise of the total magnetic energy in the gain layer $e_{\text{mag;gain}}$ is followed by a phase of a relatively constant total field energies. When taking into account the scaling of the initial fields (see the dashed lines), we find a very similar amount of field amplification for all models. This result suggests that the amplification is dominated by kinematic processes and that the back-reaction of the field onto the flow is weak. We do find, however, that the average magnetic energy of model s15-B12 is systematically lower than expected from the scaling of the initial fields (cf. Fig. 17, where the black dashed line is below the

other lines). This somewhat weaker amplification is consistent with the presence of large subalfvénic regions where the field is sufficiently strong to react back onto the flow. The Alfvén-wave amplification enhancing the field in this model compared to models with weaker initial fields affects regions that are too small to shine up in this volume-integrated energy.

Finally, we discuss the distribution of the magnetic energy in the different regions of the core as a function of initial field strength. We refer to Tab. 2 for a synopsis of our results. We compare the root-mean-square averages of the magnetic field strength in four domains:

b_{14} is the r.m.s. field in the PNS at densities above $10^{14} \text{ g cm}^{-3}$;
 b_{cnv} is the r.m.s. field in the PNS convection zone;

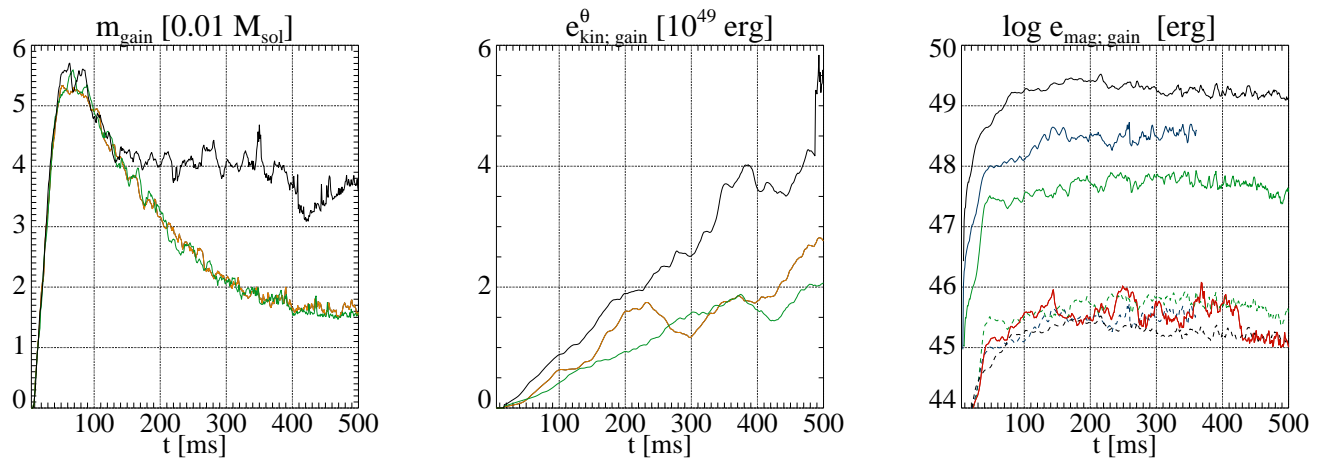


Fig. 17. *Left panel:* Mass in the gain region of models s15-B0 (orange line), s15-B11 (green line), and s15-B12 (black line) as a function of time. *Middle panel:* Lateral kinetic velocity in the gain region of models s15-B0 (orange line), s15-B11 (green line), and s15-B12 (black line) as a function of time. *Right panel:* Logarithm of the magnetic energy in the gain region of models s15-B10 (red line), s15-B11 (green line), s15-B11.5 (blue line), and s15-B12 (black line) as a function of time. The solid lines show the total magnetic energy of the models and the dashed lines (for the models with $b_0 > 10^{10}$ G) the same quantity scaled according to the initial strength, respectively.

b_{stb} is the r.m.s. field in the hydrodynamically stable region surrounding the PNS;

b_{gain} is the r.m.s. field in the gain (SASI) layer.

Additionally, we compare the ratios of magnetic to internal or kinetic energy, $\beta^{i/k}$, in the same regions.

For all domains, the mean fields increase monotonically with the initial field strength, b_0 . The maximum field is reached in the PNS. Since this region is hydrodynamically stable during the simulated evolution, amplification is dominated by radial compression. From a weak initial field, typical pulsar fields of the order of 10^{12-13} G can be achieved. With a more extreme initial field of $b_0 \sim 10^{12}$ G in the pre-collapse stellar core, we get magnetar-like values of 10^{15} G. Compared to the thermal energy, the magnetic field is negligible even for this case; it can, however, dominate over the velocity field. Since there is no feedback of the field, the final fields in the PNS core scale very well with b_0 .

In the PNS convection zone, the average field is somewhat weaker than in the core of the PNS. As discussed above, the convective velocities can become subalfvénic for the strongest fields, corresponding to a magnetic energy exceeding the kinetic energy, i.e., $\beta^k > 1$; this is the case for model s15-B12. In such a situation, the efficiency of the field amplification is limited. Consequently, the scaling of the r.m.s. field with b_0 breaks down for $b_0 \gtrsim 3 \times 10^{11}$ G. The field found for model s15-B12, $b_{\text{cns}} \approx 4.7 \times 10^{14}$ G, should be close to the maximum field that can be achieved by the PNS convection excited in this core.

Similar results can be found in the hydrodynamically stable layer between the PNS convection zone and the gain region. The r.m.s. magnetic field strength is weaker by a factor of ~ 3 . Again, we find a ratio of magnetic to kinetic energy in excess of unity for the strongest initial field considered and a deviation of the final magnetic field strength from a simple scaling with the initial field strength.

The r.m.s. field strength in the gain layer is between 3.6×10^{11} G for model s15-B10 and 1.2×10^{13} G for model s15-B12. In all models, β^k is below unity, though. As discussed in Sect. 4.2.2 and Sect. 4.3, trans- and subalfvénic regions are present and have an important influence on the dynamics and

the field amplification. Because the magnetic field strength decreases more slowly with radius than the internal energy, β^i can be as large as one per cent here.

Finally, we note that for all models by far most (of the order of two thirds) of the magnetic energy is contained in the PNS convection region. The magnetic energies in the stable layer are of the same order of magnitude as those in the gain region, though the exact value of b_{gain} is variable and depends strongly on the size of the gain region.

5. Summary and conclusions

We have studied (some of) the processes leading to the amplification of the magnetic field in a non-rotating stellar core during the collapse and post-bounce accretion phases of a supernova. In non-rotating stars, a variety of amplification mechanisms considered in previous works, e.g., winding of the field by differential rotation or the MRI, are not viable. Instead, convection and the SASI may constitute (small-scale) dynamos. Additionally, Alfvén waves travelling against the gas flow may be amplified once they reach an Alfvén point where the (co-moving) Alfvén velocity equals the gas velocity, a condition that could be fulfilled in the accretion flow onto the PNS. If efficient amplification occurs, the field may be able to affect the dynamics of the core, e.g., by altering the geometry of SASI flows or by energy dissipation through Alfvén waves in the upper layers of the hot-bubble region.

Reducing the complexity of the problem, simplified models, e.g., one-dimensional simulations with assumptions for the excitation, propagation and dissipation of Alfvén waves (Suzuki et al. 2008), toy models of Alfvén waves in decelerating flows (Guilet et al. 2010), and 2D and 3D MHD simulations without neutrino transport (Endeve et al. 2010) have demonstrated that these effects could, in principle, be relevant. On the other hand, to study their evolution under less idealised conditions, in particular their interplay with a highly dynamical background, more calculations of self-consistent models are required, i.e. multi-dimensional MHD including a treatment of neutrino transfer through the stellar core.

To this end, we have performed axisymmetric simulations of the collapse and the post-bounce evolution of the core of a star of 15 solar masses possessing a purely poloidal initial field. Using a new code for neutrino-magnetohydrodynamics, we have solved the MHD equations coupled to the system of two-moment equations for the neutrino transport; the closure for the moment equations was provided by an analytic variable Eddington factor. We included descriptions for the most important reactions between electron neutrinos and antineutrinos and the stellar matter, viz. nucleonic and nuclear emission and absorption and scattering off nucleons and nuclei. Compared to current state-of-the-art techniques such as Boltzmann codes, our approach ignores muon and tau neutrinos and is less accurate in treating neutrino-matter interactions, but needs much less computational resources and possesses full two-dimensionality including velocity effects. We are able to reproduce the basic features found in detailed simulations, e.g., the stagnation of the prompt shock wave, PNS and hot-bubble convection, and the SASI activity. Hence, our models allow for a fairly reliable assessment of the main MHD effects in self-consistent SN core models; we discuss the remaining major limitations below.

The principal results of our simulations and the main conclusions to be drawn from our results are:

1. The magnetic field is amplified kinematically by the turbulent flows developing due to convection and the SASI. The amplification factor does not depend on the initial field unless it reaches, starting from a high initial value, equipartition with the kinetic energy, the maximum possible energy attainable. The maximum field we observe is a few times 10^{15} G at the base of the PNS convection layer. In the PNS convection zone, the radial profile of the field strength can be approximated by a power law, $|b| \propto r^{-2}$.
2. When falling through the non-spherical supernova shock, the magnetic field is bent by lateral flows, creating a component parallel to the shock. These perturbations are advected towards the PNS convection zone. The field accumulates there, leading to a layer of strong magnetic fields. Since the perturbations are associated with a strong lateral component of the field, this layer is dominated by the θ -component of the field. Hence, Alfvén waves propagate at constant radius rather than upwards. Therefore, we do not find an Alfvén surface in the accretion flow, although there are sub- as well as super-alfvénic regions in this layer. This limits the efficiency of the amplification mechanism proposed by Guilet et al. (2010).
3. Conditions for the latter effect are more favourable if accretion occurs through a rather stationary column. In our axisymmetric models, this is the case mostly along the polar axis where the geometry enforces radial fields and flows. An Alfvén surface forms in the radial field of the accretion column at a radius depending on the initial field strength. For fields of $b_0 \gtrsim 10^{11}$ G initially, we observe that perturbations created in the PNS convection zone propagate along the field upwards into the accretion column. Interacting with the accretion flow, they lead to a steepening of the profile of the accretion velocity near the lower end of the accretion column to a discontinuity where a strong enhancement of the magnetic field takes place.
4. The strongest initial field we have investigated, $b_0 = 10^{12}$ G, is able to shape the post-shock flow. It favours the formation of a flow dominated by low-order multipole modes, viz. a quadrupolar pattern of accretion columns at the poles and near the equator. In the stable polar columns we observe, as in the case of lower fields ($b_0 = 10^{11}$ G), an interaction of perturbations travelling upwards from the PNS convection zone with the accretion flow. This gives rise to the formation of a layer of very strong field. Also in the convective and SASI layers behind the shock, the field strength grows with the magnitude of the initial field. In this model with its particular flow topology, we find the most pronounced shock expansion of all models.

In summary, our results suggest that magnetic field amplification to interesting strengths can efficiently take place during the stellar core collapse even in the absence of rotation. In addition to an enhancement due to compression by the radial collapse, we find that non-radial fluid flows associated with convection and SASI activity, and the interaction of Alfvén waves in the accretion flows can amplify the initial iron-core fields. Starting with 10^9 – 10^{10} G as predicted by present stellar evolution models (Heger et al. 2005), field strengths of typical pulsars (10^{12} – 10^{13} G) can be reached. Magnetar fields of 10^{14} – 10^{15} G result when the progenitor core possesses a pre-collapse field between a few 10^{11} G and 10^{12} G. Only in the latter case, the fields around the nascent neutron star obtain dynamical importance and might have an influence on the supernova explosion mechanism.

Though offering some insight into the magnetic-field evolution in non-rotating magnetised cores, our study has several important limitations:

1. We have used a new treatment of neutrino transport and simplified neutrino-matter interactions constraining ourselves to electron neutrinos and antineutrinos. While the accuracy of the transport compared to other schemes has to be assessed in a separate study, and our set of neutrino reactions is certainly insufficient for high-precision supernova physics, we do not deem this a problem for the presented investigation because we are able to capture the most important dynamical effects in a supernova core.
2. To save computational costs, we have restricted ourselves to axisymmetric simulations. In the light of the anti-dynamo theorems, this is a severe limitation leading to a wrong, possibly too low, level of amplification of the field in the turbulent regions. Furthermore, our models do not allow for the development of shear layers associated with non-axisymmetric spiral modes of the SASI, which may also be a site of efficient amplification of the magnetic field (see also Endeve et al. 2010).
3. Moreover, axisymmetry restricts the dynamics of the accretion flows, favouring the development of very stable accretion columns along the poles. As we have seen, field amplification shows very distinct features in and below these columns. We presume that the dynamics in three dimensions is dominated by what we have seen in off-axis accretion flows, i.e., less stable Alfvén surfaces and less efficient amplification of Alfvén waves. Very strong initial fields of the order of $b_0 = 10^{12}$ G lead to high field strengths that are able to dominate the post-shock accretion flow. This may establish coherent, stable accretion columns. For such fields, our axisymmetric results may hence be a decent approximation.
4. Turbulent field amplification may be very sensitive to dissipation coefficients, physical and numerical. Our models, based on *ideal* MHD, neglect dissipation by physical viscosity and resistivity, but are computed on relatively coarse numerical grids corresponding to excessive numerical dissipation. Therefore, we are not able to follow the turbulent (inverse) cascades of magnetic and kinetic energy and helicity covering many orders of magnitude in wave number in a supernova core. The effect of insufficient reso-

lution on Alfvén waves is probably less serious though their wave number should increase as they approach the an Alfvén point, requiring enhanced resolution. Simulations of cores at a resolution corresponding to numerical viscosity and resistivity below the physical ones are by far too expensive today, and will remain so for a long time. To tackle this difficulty, a combination of different approaches would be desirable, viz. global direct numerical simulations of the core with drastically enhanced physical transport coefficients, and simple sub-grid models for MHD turbulence based on idealised local simulations neglecting most aspects of, e.g., neutrino physics. We are, however, aware of the lack of reliable sub-grid models for MHD at present, obstructing further progress in this direction.

Apart from these methodological shortcomings, open physical questions are, e.g., the influence of the progenitor on the establishment of certain patterns in the accretion flow, effects of very strong initial fields, and the influence of slow rotation of the core on our findings. In particular the last issue may prove interesting as it would enable a large-scale dynamo. We defer these questions as well as the more technical problems listed above to further investigations.

Acknowledgements. HTJ is grateful to Jérôme Guilet and Thierry Foglizzo for interesting and educative discussions. M.O. is supported by a *Golda Meir Postdoctoral Fellowship* of the Hebrew University of Jerusalem. This work was supported by the Deutsche Forschungsgemeinschaft through the Transregional Collaborative Research Centers SFB/TR 27 “Neutrinos and Beyond” and SFB/TR 7 “Gravitational Wave Astronomy” and the Cluster of Excellence EXC 153 “Origin and Structure of the Universe” (<http://www.universe-cluster.de>). The simulations were performed at the Rechenzentrum Garching (RZG) of the Max Planck Society.

Appendix A: Neutrino transport

Most results on magnetic effects in supernovae draw from more or less idealised investigations, e.g., analytic calculations or simplified models focusing on one particular aspect of the problem while neglecting some of the complex physics of the explosion and, thus, limiting their range of application. Due to the enormous computational requirements of an accurate treatment of the transport of neutrinos and their interaction with matter, simplifications are most commonly made in this sector. Not discussing local simulations focusing on a high-resolution modelling of a small part of the flows, we can distinguish between different approximations:

1. Some studies (e.g., Obergaulinger et al. 2006; Mikami et al. 2008) neglect the effect of neutrinos completely and use only a simplified, e.g., polytropic, equation of state. Typically, these models exhibit prompt explosions, limiting their validity to the immediate (few milliseconds) post-bounce phase. Even without any treatment of neutrinos, it is possible to simulate the development of the SASI (e.g., Blondin et al. 2003).
2. A way to model the dynamics qualitatively correctly while avoiding the complications of a full neutrino-transport scheme is the use of simple heating/cooling or deleptonisation source terms. Such schemes prescribe the loss and gain of energy or electron number by cooling and heating terms that depend on the local thermodynamic state of the matter (e.g., density, temperature, electron fraction). Depending on the details of the model, they can reproduce, e.g., the correct deleptonisation behaviour during collapse (e.g., Liebendörfer 2005) or the development of the SASI (Fernández & Thompson 2009; Fernández 2010).

3. A leakage scheme accounts for the optical depth of the region emitting neutrinos is taken into account in the cooling terms. The results of such simulations can be similar to that of models with purely local cooling terms (e.g., Kotake et al. 2004).
4. Despite the large computational effort, various methods for energy-dependent neutrino hydrodynamics have been used; state-of-the-art codes include, e.g., the *isotropic diffusion source approximation*, a scheme decomposing the neutrinos into a trapped, diffusing, and a freely streaming component (Liebendörfer et al. 2009), flux-limited diffusion (FLD), or solve the Boltzmann equation for the neutrino phase-space distribution. Among the codes based on the FLD method, there is a wide variety of approaches to the treatment of multi-dimensional effects and the coupling of energy bins:
 - Livne et al. (2004); Burrows et al. (2007) use a multi-group FLD code without energy-bin coupling and no velocity terms in the moments equations,
 - Walder et al. (2005); Ott et al. (2008) use a two-dimensional multi-angle, multi-group FLD code without energy-bin coupling and no velocity terms in the moment equations,
 - the simulations of Mezzacappa et al. (2007); Yakunin et al. (2010) employ a *ray-by-ray-plus* multi-group FLD method that includes the energy-bin coupling terms and the velocity terms up to order $\mathcal{O}(v/c)$.

Similar distinctions can be made for the codes based on Boltzmann solvers:

- Mezzacappa & Bruenn (1993); Mezzacappa et al. (2001); Liebendörfer et al. (2004) solve the one-dimensional Boltzmann equation by an S_n technique,
- Rampp & Janka (2002) employ a one-dimensional two-moment-closure scheme with a closure relation obtained from the solution of a model Boltzmann equation,
- this scheme was generalised to a ray-by-ray-plus version by Buras et al. (2006), accounting for all terms coupling energy bins and all velocity-dependent terms. Müller et al. (2010) developed a 2D general relativistic hydro solver with a ray-by-ray-plus neutrino transport similar to Buras et al. (2006).

These schemes provide the best models of the complex flow patterns of a supernova and allow for a reliable distinction between successful and failed supernovae and an accurate prediction of the explosion energy. Testing the limits of currently available supercomputers, two-dimensional axisymmetric simulations are possible, but the step to three-dimensional models may require a profound change of algorithms and programming models to take full advantage of the next generation of computers.

Neutrino transfer describes the neutrinos in terms of their phase-space distribution function, $f(t, \mathbf{x}, \epsilon, \mathbf{n})$, a function of time, t , position, \mathbf{x} , neutrino energy, ϵ , and propagation direction, \mathbf{n} ($|\mathbf{n}| = 1$). The dimensionality of this function is the main reason for the high computational requirements of RT. It can be reduced by evolving the set of neutrino moments, $M_\nu^k = \int d\Omega \mathbf{n}^k f$, $k = 0, \dots, \infty$, rather than the distribution function; the first moments have an immediate physical meaning: $k = 0, 1, 2$ correspond to the neutrino energy density, momentum density, and pressure tensor, respectively.

In principle, the full infinite series of moments is required for an accurate representation of f . In practise, the series is trun-

cated at some level, k_{\max} , retaining the conservation laws for the first few moments. Since the equation for the k^{th} moment,

$$\partial_t M_\nu^k + \nabla M_\nu^{k+1} = Q_\nu^k, \quad (\text{A.1})$$

involves at least the next moment (order $k + 1$), a closure is required to relate the first moment beyond truncation, $M_\nu^{k_{\max}+1}$, to the moments of order $0, \dots, k_{\max}$ (the source term, Q_ν^k , accounts for all interaction terms and for velocity-dependent terms such as advection, compression, or Doppler shifts). A common choice is the 0^{th} -moment system, the equation for the neutrino energy, with the first moment given by the (flux-limited) diffusion flux. We go one step beyond this and evolve the 1^{st} -moment system,

$$\partial_t E_\nu + \nabla F_\nu = Q_\nu^0, \quad (\text{A.2})$$

$$\partial_t F_\nu + \nabla P_\nu = Q_\nu^1, \quad (\text{A.3})$$

closing the system by assuming a simple analytic form of the 2^{nd} moment, $P_\nu = P_\nu(E_\nu, F_\nu)$. In a one-dimensional system, one scalar function is sufficient to define the closure, the *Eddington factor* p_ν . Following Audit et al. (2002), we construct a tensorial closure for multi-dimensional systems from the one-dimensional Eddington factor:

$$P_\nu^{ij} = \left(\frac{1 - p_\nu}{2} \delta^{ij} + \frac{3p_\nu - 1}{2} \frac{F_\nu^i F_\nu^j}{F_\nu^2} \right) E_\nu. \quad (\text{A.4})$$

This expression combines a diagonal part, accounting for isotropic diffusion, with a contribution accounting for free streaming in the direction of the neutrino flux. In the diffusion limit, the Eddington factor is $p_\nu = 1/3$, and the pressure tensor is given by the isotropic part alone, $P_\nu^{ij} = E_\nu/3 \delta^{ij}$, and in the free-streaming limit, $p_\nu = 1$, only the second part contributes, the total neutrino pressure is E_ν and P_ν^{ij} is peaked in the propagation direction of the neutrinos. Pons et al. (2000) have demonstrated the applicability of standard HRSC methods to this (hyperbolic) system and compared different suggestions for the closure. In our simulations, we use the Eddington factor by Minerbo (1978). To avoid the evaluation of the Langevin function in the expression for the closure, we apply a simple polynomial approximation given by Cernohorsky & Bludman (1994):

$$p_\nu = \frac{1}{3} + \frac{1}{15} (6f_\nu^2 - 2f_\nu^3 + 6f_\nu^4), \quad (\text{A.5})$$

where $f_\nu = F_\nu/cE_\nu$ is the flux factor of the neutrinos, i.e., the neutrino flux normalised to the maximum flux allowed by causality.

Exploiting the hyperbolic character of the RT system, we use HRSC methods for the moments equations, viz. the same high-order reconstruction as in the MHD subsystem, either the Lax-Friedrichs or the HLL approximate Riemann solver, and an explicit Runge-Kutta time integrator. This approach meets its limitations when the Peclet number, $\text{Pe} = \chi^1 \delta x$, i.e., the optical depth of one grid cell of width δx (c is the speed of light), exceeds one. Then, the interaction source term of the neutrino fluxes, $-c\chi^1 F_\nu$, becomes stiff (the characteristic time scale being $\sim 1/(c\chi)$), enforcing a time step much below that of the hyperbolic MHD or transport parts, $(\delta t)_{\text{hyp}} \leq \delta x/c_{\max}$, for a given maximum characteristic speed c_{\max} . Similarly to Pons et al. (2000) and Audit et al. (2002), we modify the Riemann fluxes of the 0^{th} moments to reproduce the correct parabolic diffusion limit and use an implicit time integrator for the interaction source term of the first moment, thereby avoiding a time-step restriction below $(\delta t)_{\text{hyp}}$. A stiff part of the system on its own if $c\chi^0 \delta t > 1$, the

neutrino-matter interaction source terms in the 0^{th} -order moment equation are treated implicitly as well.

Including contributions due to the fluid velocity of order $O(v/c)$, we solve the equations for the neutrino moments in the *co-moving* frame of reference, summarised, e.g., by Munier & Weaver (1986) (ω is the neutrino energy):

$$\partial_t E_\nu + \nabla \cdot (E_\nu \mathbf{v} + \mathbf{F}_\nu) - \omega \nabla_j \nu_k \partial_\omega P_\nu^{jk} = S_\nu^0, \quad (\text{A.6})$$

$$\partial_t F_\nu^i + \nabla_j (F_\nu^i \nu^j + P_\nu^{ij}) + F_\nu^i \nabla_j \nu^j = S_\nu^{1:i}. \quad (\text{A.7})$$

In these equations, we have separated the total source terms, $Q_\nu^{0,1}$ (Eq. (A.2) and Eq. (A.3)), into source terms due to neutrino-matter reactions, $S_\nu^{0,1}$, and velocity-dependent terms. We ensure the simultaneous conservation of neutrino energy and number density by evolving a duplicate set of neutrino moments for both conserved variables. There are alternatives to this approach, e.g., using a consistent discretisation of the neutrinos in energy space (Müller et al. 2010).

Striving for simplification of our modelling, we include a reduced set of neutrino-matter interactions only. It consists of

1. emission and absorption of electron neutrinos by neutrons,
2. emission and absorption of electron anti-neutrinos by protons,
3. elastic scattering of all neutrino flavours off nucleons,
4. emission and absorption of electron neutrinos by heavy nuclei,
5. coherent elastic scattering of all neutrino flavours off heavy nuclei.

The reaction rates and opacities are implemented following Rampp & Janka (2002). Neglecting pair processes, we do not create μ and τ neutrinos. Furthermore, we neglect inelastic scattering of neutrinos off leptons. From these reactions, we can construct the source terms of the 0^{th} and 1^{st} moments,

$$S_\nu^0 = c\chi^0 (E_\nu^{\text{eq}} - E_\nu), \quad (\text{A.8})$$

$$S_\nu^1 = -c\chi^1 F_\nu, \quad (\text{A.9})$$

where E_ν^{eq} is the equilibrium (Fermi-Dirac) value of the 0^{th} moment. The opacities for the 0^{th} and 1^{st} moments include absorption and emission processes only and absorption, emission, and scattering processes, respectively.

The number of neutrinos in a certain energy bin is limited by the Pauli exclusion principle. If a bin is populated by a number of neutrinos close to this limit, interactions, in particular inelastic scattering, redistributing the particles in energy space, are getting phase-space blocked such that a violation of the Pauli principle is avoided. Numerical schemes solving the interaction terms and the spatial derivatives of the transport equations time-implicitly, obey this constraint naturally. Since we are using an explicit time integrator for the spatial derivatives instead, we have to enforce this constraint manually similarly to Swesty & Myra (2005).

References

- Akiyama, S., Wheeler, J. C., Meier, D. L., & Lichtenstadt, I. 2003, *ApJ*, 584, 954
- Audit, E., Charrier, P., Chièze, J., & Dubroca, B. 2002, *ArXiv Astrophysics e-prints*
- Bisnovatyi-Kogan, G. S., Popov, I. P., & Samokhin, A. A. 1976, *Ap&SS*, 41, 287
- Blondin, J. M., Mezzacappa, A., & DeMarino, C. 2003, *ApJ*, 584, 971
- Brandenburg, A. & Subramanian, K. 2005, *Astronomische Nachrichten*, 326, 400
- Buras, R., Rampp, M., Janka, H.-T., & Kifonidis, K. 2006, *A&A*, 447, 1049

- Burrows, A., Dessart, L., Livne, E., Ott, C. D., & Murphy, J. 2007, *ApJ*, 664, 416
- Burrows, A., Livne, E., Dessart, L., Ott, C. D., & Murphy, J. 2006, *ApJ*, 640, 878
- Cerdá-Durán, P., Font, J. A., Antón, L., & Müller, E. 2008, *A&A*, 492, 937
- Cerdá-Durán, P., Font, J. A., & Dimmelmeier, H. 2007, *A&A*, 474, 169
- Cernohorsky, J. & Bludman, S. A. 1994, *ApJ*, 433, 250
- Cernohorsky, J. & van Weert, C. G. 1992, *ApJ*, 398, 190
- Dessart, L., Burrows, A., Livne, E., & Ott, C. D. 2006, *ApJ*, 645, 534
- Endeve, E., Cardall, C. Y., Budiardja, R. D., & Mezzacappa, A. 2010, *ApJ*, 713, 1219
- Evans, C. R. & Hawley, J. F. 1988, *ApJ*, 332, 659
- Fernández, R. 2010, *ArXiv e-prints*
- Fernández, R. & Thompson, C. 2009, *ApJ*, 697, 1827
- Foglizzo, T. 2001, *A&A*, 368, 311
- Foglizzo, T. 2002, *A&A*, 392, 353
- Guilet, J., Foglizzo, T., & Fromang, S. 2010, *ArXiv e-prints*
- Heger, A., Woosley, S. E., & Spruit, H. C. 2005, *ApJ*, 626, 350
- Kotake, K., Sawai, H., Yamada, S., & Sato, K. 2004, *ApJ*, 608, 391
- Liebendörfer, M. 2005, *ApJ*, 633, 1042
- Liebendörfer, M., Messer, O. E. B., Mezzacappa, A., et al. 2004, *ApJS*, 150, 263
- Liebendörfer, M., Whitehouse, S. C., & Fischer, T. 2009, *ApJ*, 698, 1174
- Livne, E., Burrows, A., Walder, R., Lichtenstadt, I., & Thompson, T. A. 2004, *ApJ*, 609, 277
- Marek, A., Dimmelmeier, H., Janka, H.-T., Müller, E., & Buras, R. 2006, *A&A*, 445, 273
- Marek, A. & Janka, H. 2009, *ApJ*, 694, 664
- Meier, D. L., Epstein, R. I., Arnett, W. D., & Schramm, D. N. 1976, *ApJ*, 204, 869
- Meynet, G., Eggenberger, P., & Maeder, A. 2011, *A&A*, 525, L11+
- Mezzacappa, A. & Bruenn, S. W. 1993, *ApJ*, 405, 669
- Mezzacappa, A., Bruenn, S. W., Blondin, J. M., Hix, W. R., & Bronson Messer, O. E. 2007, in *American Institute of Physics Conference Series*, Vol. 924, *The Multicolored Landscape of Compact Objects and Their Explosive Origins*, ed. T. di Salvo, G. L. Israel, L. Piersant, L. Burderi, G. Matt, A. Tornambe, & M. T. Menna, 234–242
- Mezzacappa, A., Liebendörfer, M., Messer, O. E., et al. 2001, *Physical Review Letters*, 86, 1935
- Mikami, H., Sato, Y., Matsumoto, T., & Hanawa, T. 2008, *ApJ*, 683, 357
- Minerbo, G. N. 1978, *J. Quant. Spec. Radiat. Transf.*, 20, 541
- Miyoshi, T. & Kusano, K. 2005, *Journal of Computational Physics*, 208, 315
- Müller, B., Janka, H., & Dimmelmeier, H. 2010, *ApJS*, 189, 104
- Munier, A. & Weaver, R. 1986, *Computer Physics Reports*, 3, 165
- Obergaulinger, M., Aloy, M. A., & Müller, E. 2006, *A&A*, 450, 1107
- Obergaulinger, M., Cerdá-Durán, P., Müller, E., & Aloy, M. A. 2009, *A&A*, 498, 241
- Ott, C. D., Burrows, A., Dessart, L., & Livne, E. 2008, *ApJ*, 685, 1069
- Pons, J. A., Ibáñez, J. M., & Miralles, J. A. 2000, *MNRAS*, 317, 550
- Rampp, M. & Janka, H.-T. 2002, *A&A*, 396, 361
- Scheidegger, S., Fischer, T., Whitehouse, S. C., & Liebendörfer, M. 2008, *A&A*, 490, 231
- Shen, H., Toki, H., Oyamatsu, K., & Sumiyoshi, K. 1998, *Progress of Theoretical Physics*, 100, 1013
- Suresh, A. & Huynh, H. 1997, *J. Comput. Phys.*, 136, 83
- Suwa, Y., Takiwaki, T., Kotake, K., & Sato, K. 2007, *PASJ*, 59, 771
- Suzuki, T. K., Sumiyoshi, K., & Yamada, S. 2008, *ApJ*, 678, 1200
- Swesty, F. D. & Myra, E. S. 2005, in *Open Issues in Core Collapse Supernova Theory*, ed. A. Mezzacappa & G. M. Fuller, 176–+
- Symbalisty, E. M. D. 1984, *ApJ*, 285, 729
- Thompson, C. & Duncan, R. C. 1993, *ApJ*, 408, 194
- Titarev, V. A. & Toro, E. F. 2005, *International Journal for Numerical Methods in Fluids*, 49, 117
- Walder, R., Burrows, A., Ott, C. D., et al. 2005, *ApJ*, 626, 317
- Woosley, S. E., Heger, A., & Weaver, T. A. 2002, *Reviews of Modern Physics*, 74, 1015
- Yakunin, K. N., Marronetti, P., Mezzacappa, A., et al. 2010, *Classical and Quantum Gravity*, 27, 194005